On the evolution and saturation of instabilities of two-dimensional isolated circular vortices

By R. C. KLOOSTERZIEL[1] AND G. F. CARNEVALE[2]

[1] School of Ocean and Earth Science and Technology, University of Hawaii at Manoa, Honolulu, HI 96822, USA

[2] Scripps Institution of Oceanography, University of California San Diego, La Jolla, CA 92093, USA

Laboratory observations and numerical experiments have shown that a variety of compound vortices can emerge in two-dimensional flow due to the instability of isolated circular vortices. The simple geometrical features of these compound vortices suggest that their description may take a simple form if an appropriately chosen set of functions is used. We employ a set which is complete on the infinite plane for vorticity distributions with finite total enstrophy. Through projection of the vorticity equation (Galerkin method) and subsequent truncation we derive a dynamical system which is used to model the observed behaviour in as simple as possible a fashion. It is found that at relatively low-order truncations the observed behaviour is qualitatively captured by the dynamical system. We determine what the necessary ingredients are for saturation of instabilities at finite amplitude in terms of wave–wave interactions and feedback between various azimuthal components of the vorticity field.

1. Introduction

In two-dimensional or quasi-geostrophic fluid dynamics several types of coherent flow structures have been discovered in recent years. The most common is the simple monopolar vortex, often circularly symmetric in the absence of external strain. Such vortices emerge in two-dimensional turbulence from an initial state of randomly distributed vorticity due to the spectral flux of kinetic energy to larger scales (McWilliams 1984; Sadourny 1985; Benzi, Patarnello & Santangelo 1988). Chance encounters of such vortices with oppositely-signed circulations can lead to the formation of a dipole which is a self-propelling compound vortex. In forced two-dimensional turbulence, Legras, Santangelo & Benzi (1988) observed a coherent compound vortex of an even more complicated nature, the so-called tripole. Laboratory experiments (van Heijst & Kloosterziel 1989) and numerical simulations (Carton, Flierl & Polvani 1989) showed tripole formation due to the growth of an azimuthal wavenumber-2 instability of an unstable isolated circular vortex. Laboratory experiments revealed that wavenumber-3 instabilities can lead to an even more complicated compound vortex, called the triangular vortex (see Kloosterziel & van Heijst 1991). Carnevale & Kloosterziel (1994) and Morel & Carton (1994) investigated whether compound vortices could result from instabilities associated with even higher azimuthal wavenumbers. This was found unlikely because these vortices are unstable to infinitesimally small perturbations. The tripole and triangular vortex have simple symmetric vorticity distributions. This suggests that these vorticity patterns can be closely approximated by sums of a

small number of appropriately chosen functions and that the dynamics describing the evolution may possibly be modelled in a simple fashion. These issues are addressed in this paper. Three instabilities are analysed. In each case a circular vortex is initially slightly perturbed. Which instability ensues depends on the particular initial axisymmetric vorticity distribution and on of what kind the initial perturbation is. First we consider tripole and triangular vortex formation and then a third instability which leads to what we call a square vortex. Like the tripole and the triangular vortex, it is a rotating compound vortex. But it is unstable and breaks up into two dipoles. In §2.1 we present graphs from numerical simulations showing these instabilities. In §2.2 the vorticity fields ω are decomposed into an axisymmetric component ω_0 and azimuthal deviations $\omega_{k>0}$, i.e. $\omega = \sum_k \omega_k$ with $k = 0, 1, 2, \dots$. A different fundamental azimuthal wavenumber $k = m$ is associated with each of the compound vortices. The most unstable normal modes for the circular flows that give rise to them are obtained by filtering the ω_m-component from the numerical data at early stages in the evolution. We determine the temporal evolution of the components and show that there is a strict hierarchy in their amplitudes and that only a small number of azimuthal components ω_k dominate during the evolution.

In §3 we derive through projection of the vorticity equation (Galerkin method) and truncation a finite-dimensional dynamical system. Numerous studies in all areas of physics have employed this method. The best known example of a dynamical system thus derived is the celebrated Lorenz (1963) model. It has not been used before to gain a better understanding of the evolution of two-dimensional vortices, in particular the seemingly complex metamorphosis from circular to compound. It differs also from previous studies in that we apply it to the evolution on an infinite domain. Usually box-like or compact domains like a sphere are considered and expansions in eigenfunctions of the Laplace operator are used. On such domains the eigenvalues (e.g. wavenumbers) of the Laplacian are discrete, and a spectral truncation usually involves eliminating all modes of length scale smaller than some prescribed value. On the infinite plane, however, the spectrum is continuous. Sums over the eigenfunctions are replaced by integrals and truncation of the integrals at a given length scale still leaves an infinite number of modes to deal with, that is, no finite-dimensional system can be derived by truncation. We can resolve this dilemma by abandoning the requirement that the functions in which the fields are expanded be eigenfunctions of the Laplacian operator. Any complete orthogonal set of functions that span the plane could be used. We use functions which are not eigenfunctions of the Laplace operator. A low-order model can be obtained by truncation because they form a discrete set. Vortices with finite total enstrophy can be represented by an expansion $\omega = \sum_n \sum_k b_n^k(t) \varphi_n^k(r, \theta)$ with the φ_n^k essentially of the form $\varphi_n^k(r, \theta) = f_n(r) e^{ik\theta}$. Cylindrical polar coordinates (r, θ) are used with the origin $(r = 0)$ at the centre of the initially axisymmetric vortex. The radial part f_n is a Laguerre function which consists of a polynomial in r times an exponentially decaying part. The order of the polynomial is higher as n increases. The projection leads to a system of coupled ordinary differential equations for the expansion coefficients $b_n^k(t)$. The advection term of the vorticity equation appears as quadratic terms in the expansion coefficients b_n^k multiplied by nonlinear interaction coefficients. A finite-dimensional dynamical system is obtained by limiting the azimuthal wavenumbers k and radial wavenumbers n to finite ranges. This system provides a tool to systematically explore the possibility of simplifying the dynamics of compound vortex formation.

In §3.1 we determine the linear stability properties of various initial conditions in the truncated dynamical system and compare this with the relevant results from §2. It

establishes what are the smallest systems that can model the initial stages of unstable normal modes growth. We discuss the nonlinear dynamics at low-order truncations in §3.2. Emphasis is on tripole formation because triangular vortex and square vortex formation are entirely analogous. Particular attention is paid to what the necessary ingredients are for saturation at finite amplitude, in terms of feedback between various azimuthal components ω_k and the generation of higher harmonics. It is found that the first harmonic ω_{2m} is of fundamental importance in the formation process, but only for a limited time. Laplacian diffusion is further used to mimic the flow of enstrophy to smaller scales which are not resolved at low-order truncations. Through an example we show that this diminishes shape vacillations of the pattern not unlike those observed in the laboratory and high-resolution experiments. Asymptotically the system converges to a stable periodic solution. Finally, in §3.3 we discuss theory and techniques for finding time-periodic solutions in the dynamical system which correspond to steadily rotating compound vortices. We show that typically the structure of the fundamental component ω_m for a fully-formed compound vortex is close to that of one of the neutrally stable modes for its axisymmetric component ω_0. In §4 the main results and conclusions are summarized and some open questions are mentioned. Appendix A outlines how to calculate the interaction coefficients. In Appendix B it is shown that enstrophy is conserved by the system in the inviscid limit, irrespective of the chosen truncation.

2. Stability and instability of circular vortices

The stability of steady two-dimensional flows is usually determined with a normal-modes analysis of the linearized vorticity equation. Introducing a streamfunction ψ, we have in polar coordinates (r, θ) $u = r^{-1}\partial_\theta\psi$, $v = -\partial_r\psi$, and $\omega = -\nabla^2\psi$, where u and v are the radial and azimuthal velocity, respectively. For a normal modes analysis of a circular vortex the streamfunction is written as a sum of the basic steady circular flow plus a time-dependent perturbation: $\psi(r, \theta; t) = \bar{\psi}(r) + \psi'(r, \theta; t)$, where t is time. The origin $(r = 0)$ is put at the centre of the initially circular vortex. Normal modes are of the form

$$\psi'(r, \theta; t) = \mathrm{e}^{\mathrm{i}\lambda t}\phi(r)\mathrm{e}^{\mathrm{i}k\theta}. \tag{1}$$

The evolution of the real part of (1) is the physically relevant part. Small perturbations of this form make the originally circular streamlines slightly undulated when $k \neq 0$. Substitution in the inviscid two-dimensional vorticity equation and linearization yields a well-known eigenvalue problem (see Drazin & Reid 1981):

$$\left(\lambda + k\frac{\bar{v}(r)}{r}\right)\left(\frac{1}{r}\frac{\mathrm{d}}{\mathrm{d}r}r\frac{\mathrm{d}\phi(r)}{\mathrm{d}r} - \frac{k^2}{r^2}\phi(r)\right) - \frac{k}{r}\frac{\mathrm{d}\bar{\omega}(r)}{\mathrm{d}r}\phi(r) = 0. \tag{2}$$

Here $\bar{v}(r)$ is the azimuthal (swirling) velocity of the circularly symmetric vortex and $\bar{\omega}(r)$ the corresponding vorticity. A numerical method to solve this eigenvalue problem on the infinite domain is described by Gent & McWilliams (1986). When an eigenvalue λ is real, there is neutral stability with respect to a perturbation of type (1). When $\mathrm{Im}(\lambda) < 0$ it will grow exponentially, i.e. we have instability ($\mathrm{Im}(\cdot)$ denotes imaginary part). After some manipulations of (2) Rayleigh's inflection-point theorem follows: a necessary condition for having a mode with a corresponding λ for which $\mathrm{Im}(\lambda) \neq 0$ is that $\mathrm{d}\bar{\omega}/\mathrm{d}r$ changes sign somewhere (Drazin & Reid 1981). The absence of an inflection point implies neutral stability. Dritschel (1988) and Carnevale & Shepherd (1990) showed that circular vortices with no inflection point and vanishing vorticity $\bar{\omega}(r)$ for large r are in fact stable with respect to finite-sized
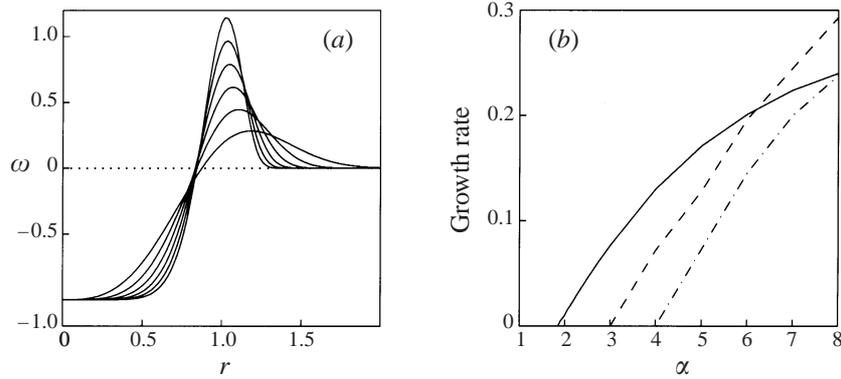
FIGURE 1. (*a*) The family of circular vortices (3) for $\alpha = 3, 4, 5, 6, 7, 8$ and (*b*) non-dimensional growth rates as a function of α for the most unstable normal modes with wavenumbers $k = 2$ (solid), $k = 3$ (dashed) and $k = 4$ (dash-dotted).

perturbations. Such vortices have circulation, i.e. their velocity $\bar{v}(r) \propto 1/r$ for $r \to \infty$. We are interested in isolated vortices for which $r\bar{v}(r) \to 0$ as $r \to \infty$. This implies that $\int_0^\infty \bar{\omega}(r) r \, dr = 0$. For such vortices $d\bar{\omega}(r)/dr$ always changes sign somewhere if $\bar{\omega}$ is a continuous function of r. An inflection point does not imply instability, it only singles out the possibly unstable candidates. Carton & McWilliams (1989) investigated the stability of circular vortices with

$$\bar{\omega}_\alpha(r) = (\tfrac{1}{2}\alpha r^\alpha - 1)e^{-r^\alpha}. \tag{3}$$

For $\alpha > 0$ they all have an inflection point. Profiles for several α-values are shown in figure 1(*a*). Below we will frequently refer to this family of vortices. The corresponding velocity profiles $\bar{v}_\alpha(r) = -\tfrac{1}{2}r \exp(-r^\alpha)$ (not shown) increase from zero at $r = 0$ to a maximum at some $r = r_{\max}$ and then fall off monotonically to zero and more rapidly so for larger α. The flow is everywhere clockwise. The vorticity is negative near the centre and positive further out. For small-enough positive α these vortices are linearly stable. For approximately $\alpha > 1.85$ they first become unstable to perturbations with $k = 2$. Carnevale & Kloosterziel (1994) plotted the growth rates of the most unstable normal modes as a function of α for wavenumbers $k = 2, 3$ and 4. An improved version of that figure is shown here as figure 1(*b*). We have increased the range of α and increased the resolution used in the calculation of the growth rates. Figure 1(*b*) shows that for large enough α several azimuthal wavenumbers can simultaneously be unstable.

If the initial perturbation is small, excited unstable modes grow initially in a fashion dictated by the linear dynamics. What happens due to nonlinear effects when amplitudes get large can be answered by solving the vorticity equation numerically. The method of simulation we used is that of Patterson & Orszag (1971) on a doubly periodic domain of $N \times N$ grid points. We employed an isotropic spectral truncation at wavenumber $k_{\mathrm{trunc}} = (8/9)^{1/2}N/2$, with a resolution $N = 256$. The factor $(8/9)^{1/2}$ derives from geometrical considerations for avoiding alias errors simultaneously involving two orthogonal directions on a square lattice. This truncation is optimal for preserving as many spatial Fourier modes as possible in an isotropically truncated spectral model. See Patterson & Orszag (1971) for a derivation of this result. Hyperviscosity was used to prevent build-up of small-scale enstrophy due to the finite resolution while keeping the energy decay at negligible levels. That is, a dissipative term of the form $v_4(\nabla^2)^2\omega$ was added to the vorticity equation. ∇^2 is the Laplace

operator here. The coefficient used was $v_4 = 4Q^{1/2}/k_{\mathrm{trunc}}^4$, where Q is the enstrophy. In our experience this hyperviscosity adequately diffuses the small scales produced in these simulations without affecting the scales of interest. The coefficient was adjusted in time as the enstrophy decayed. Time was scaled by $|\bar{\omega}(0)|^{-1}$ in the simulations discussed below. Two types of initial vorticity perturbations have been used by us and others to excite instabilities:

$$\omega' = \eta \exp\left[\frac{-(\alpha r^\alpha - 2)^2}{2\sigma^2}\right] - c, \quad \omega' = \mu \cos(k\theta) \exp\left[\frac{-(\alpha r^\alpha - 2)^2}{2\sigma^2}\right]. \qquad (4a,b)$$

In (4a) $\eta(x,y)$ is a random number uniformly generated in the range $(-\eta_0, \eta_0)$ for each grid point, and c is a constant chosen to ensure that the spatially integrated value of ω' vanishes. This perturbation is concentrated at the radius where $\bar{\omega}(r)$ of type (3) changes sign, and σ can be adjusted to make the perturbation penetrate the core of negative vorticity and the surrounding annulus of positive vorticity to any degree. In (4b) μ is a constant and k an azimuthal wavenumber.

2.1. *Examples*

According to figure 1(b) a vortex with $\alpha = 3$ is unstable to wavenumber-2 perturbations. When this vortex is randomly perturbed (perturbation of type (4a)), a wavenumber-2 instability emerges (Orlandi & van Heijst 1992). In figure 2 we show snapshots from one of our numerical simulations. The initial condition at $t = 0$ shown in panel (a) is the $\alpha = 3$ vortex with a small perturbation of type (4b) with $k = 2$ added to it. In figure 2(b) the elongated shape of the negative core vorticity indicates that at $t = 25$ a $k = 2$ mode has attained an appreciable amplitude. Two semicircular regions of positive vorticity have formed ('satellites') at $t = 50$ around which tendrils of core vorticity have been wrapped (figure 2c). Thin core vorticity filaments are observed at $t = 75$ (figure 2d) as the wrapping and stretching continues. The core is almost circular but returns to an elliptical shape as time increases to $t = 100$ (figure 2e). At this time a saturation into a 'tripole' is observed which persists afterwards. Tripole formation in a rotating homogeneous fluid is discussed by van Heijst, Kloosterziel & Williams (1991) and in a stratified fluid by Flor & van Heijst (1996). Tripoles have also been observed in the ocean (Pingree & Le Cann 1992). For a detailed numerical study see Carton & Legras (1994). The tripole of figure 2(e) rotates clockwise about its centre. Between $t = 100$ and $t = 200$ (figures 2e and 2f, respectively) it has made slightly more than one full turn. The rotation persists and the flow is quasi-stationary in a co-rotating frame, i.e. only some small erratic changes occur in the vorticity distribution. The simulation was continued until $t = 600$ and the tripole made an additional six full turns. Energy is conserved to the fourth significant digit whereas enstrophy decays roughly 5% between $t = 0$ and $t = 200$ and an additional 5% between $t = 200$ and $t = 600$.

For $\alpha > 3$ in (3), the vortex is unstable to perturbations with various azimuthal wavenumbers (see figure 1b). A random perturbation can therefore initiate the simultaneous growth of two or more modes with different azimuthal wavenumbers. For small enough perturbation amplitudes there is still a range of α-values > 3 where tripole formation occurs although $k = 3$ also grows. For example for $\alpha = 4$ there is a substantial difference between the growth rates of the most unstable modes with $k = 2, 3$. If a perturbation projects roughly equally on both modes and amplitudes need to grow 100-fold before nonlinear effects take hold, then the $k = 3$ amplitude will at that point be an order of magnitude smaller than the $k = 2$ amplitude. Tripole formation then proceeds in spite of the presence of the $k = 3$ component. Compound

(a)   (b)   (c)

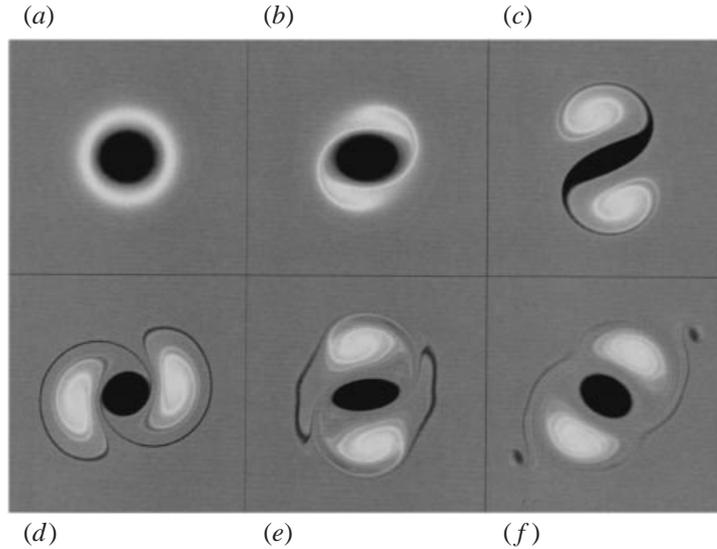(d)   (e)   (f)

FIGURE 2. Shaded contour plots of vorticity in a numerical simulation of the evolution of $\bar{\omega}_{\alpha=3}$ initially perturbed with a perturbation of type (4b) with $k = 2$, $\mu = 0.1$, $\sigma = 0.25$. Non-dimensional times are (a) $t = 0$, (b) $t = 25$, (c) $t = 50$, (d) $t = 75$, (e) $t = 100$ and (f) $t = 200$. The (non-dimensional) computational box size is 10×10. The resolution is 256^2. Uniform grey away from the central region indicates zero vorticity, black and darker grey indicate negative vorticity, white and lighter grey indicate positive vorticity.

vortices different from the tripole can form for $\alpha > 3$ when the initial perturbation is sufficiently dominated by an azimuthal wavenumber $k \neq 2$. Figure 3 shows the evolution of the $\alpha = 7$ vortex seeded with a small $k = 3$ perturbation of type (4b). The initial condition is in figure 3(a). In figure 3(b) the growth of a wavenumber-3 instability is visible. In figure 3(c) the core has become triangular while three satellites have formed around which thin filaments of core vorticity are wrapped, similar to that shown in figure 2(d) for the tripole. In figure 3(d) the final state is shown. The triangular vortex rotates about its centre without significant changes in shape. Carnevale & Kloosterziel (1994) and Beckers & van Heijst (1998) presented photographs showing triangular vortex formation in a rotating fluid. In figure 4 snapshots are shown of the evolution of the $\alpha = 7$ vortex seeded with a $k = 4$ perturbation of type (4b). Figure 4(a) shows the still roughly circular vorticity distribution at $t = 10$. At $t = 45$ (figure 4b) the core has become square in shape and four satellites have formed. The square vortex rotates but it is unstable. The onset of the instability is seen in figure 4(c) when the satellites move towards each other in pairs, and start to merge (figure 4d). The core becomes elongated (figure 4e) and breaks up into two pieces (figure 4f). Two dipoles form which propagate away in opposite directions. For laboratory experiments showing such dipole splitting events see Kloosterziel & van Heijst (1991) and Carnevale & Kloosterziel (1994). No square vortex formation has ever been observed in the laboratory (See *Note Added in Proof*, p. 256).

2.2. *Decomposition in azimuthal components*

Vorticity fields like those shown in figures 2, 3 and 4 can be expressed as $\omega = \sum_{k=0}^{\infty} \omega_k$ where

$$\omega_k = f_k(r;t)\,\mathrm{Re}\,(\mathrm{e}^{ik\theta + i\phi_k(r;t)}) \tag{5}$$
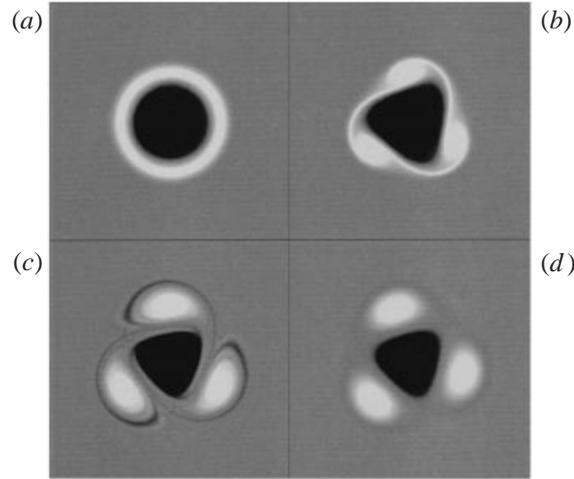
FIGURE 3. Shaded contour plots of vorticity in a numerical simulation of the evolution of $\bar{\omega}_{\alpha=7}$ initially perturbed with a perturbation of type (4b) with $k = 3$, $\mu = 0.1$, $\sigma = 0.5$. Times are (a) $t = 0$, (b) $t = 20$, (c) $t = 40$ and (d) $t = 200$. Box sizes, resolution and shading are as in figure 2.

(Re($\cdot$) denotes real part) and $\phi_k = 0$ for $k = 0$. The $f_k(r;t)$ and the phase factors can numerically be determined using $C_k = f_k \cos \phi_k$, $S_k = -f_k \sin \phi_k$ with

$$\{C_k(r;t), S_k(r;t)\} = \frac{1}{\pi} \int_0^{2\pi} \omega(r, \theta; t) \{\cos k\theta, \sin k\theta\} \, \mathrm{d}\theta. \tag{6}$$

This gives a decomposition of the vorticity distribution in azimuthal components ω_k. A measure for the amplitude of ω_k at a given time is

$$A_k(t) = Q_k^{1/2} = \left(\int_0^{2\pi} \int_0^{\infty} \omega_k^2(r, \theta; t) r \mathrm{d}r \mathrm{d}\theta \right)^{1/2}, \tag{7}$$

where Q_k is the enstrophy associated with wavenumber k. The integral converges rapidly because the vorticity amplitudes drop quickly off to zero for large r, and the actual integral is taken over the finite-sized computational domain. The origin ($r = 0$) is at the centre of the vortex.

In figure 5(a) we show the evolution of $A_k(t)$ for various even wavenumbers k in the experiment of figure 2. A similar graph was shown by Carton & Legras (1994). Amplitudes with odd k remained negligibly small. Amplitudes for $k > 8$ are at all times smaller than $A_8(t)$. At $t = 0$ A_0 is $O(1)$, A_2 is initially $O(10^{-1})$. Numerical inaccuracies due to the rather crude integration algorithm used to evaluate (6) lead to non-zero but very small amplitudes for all other wavenumbers at $t = 0$. On the logarithmic scale of figure 5(a) there is after a brief transient initially a linear increase for $k = 2$. This is the period of exponential growth of unstable $k = 2$ normal modes as in the linearized dynamics. The higher harmonics also grow, which is a nonlinear effect. Around $t = 50$ the $k = 2, 4, 6, 8$ amplitudes peak. Small oscillations appear in all A_k which persist up to $t = 300$ and beyond (not shown). The relative maximum in A_2 at $t = 50$ is when in figure 2(c) the core has become highly elongated. The following relative minimum at $t = 75$ is when in figure 2(d) the core is momentarily far less elongated. The levels about which the amplitudes oscillate afterwards correspond roughly to the vorticity distribution shown in figure 2(f).

In figure 5(b) $A_k(t)$ are shown for the experiment of figure 3, with $k = 0, 3, 6, 9, 12$

(*a*)   (*b*)   (*c*)

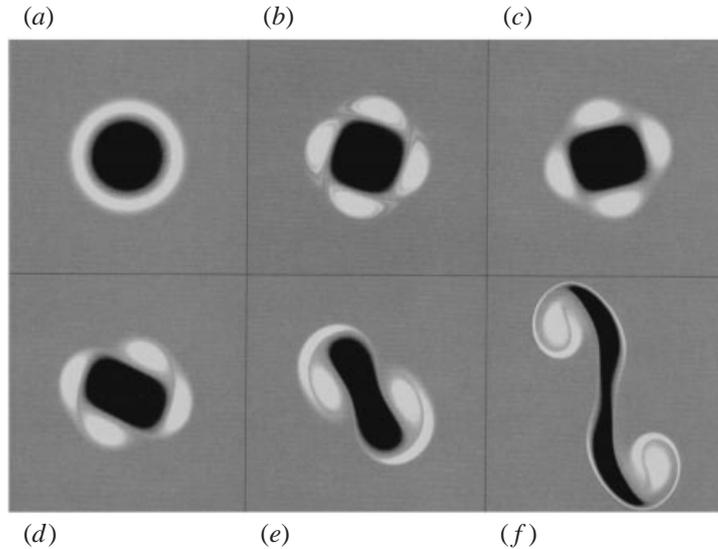(*d*)   (*e*)   (*f*)

FIGURE 4. Shaded contour plots of vorticity in a numerical simulation of the evolution of $\bar{\omega}_{\alpha=7}$ initially perturbed with a perturbation of type (4*b*) with $k = 4$, $\mu = 0.05$, $\sigma = 0.5$. Times are (*a*) $t = 10$, (*b*) $t = 45$, (*c*) $t = 152$, (*d*) $t = 157$, (*e*) $t = 163$ and (*f*) $t = 172$. Box sizes, resolution and shading are as in figure 2.

and $A_2(t)$. The evolution is similar to that shown in figure 5(*a*), except that when the final triangular vortex has formed (see figure 3*d*) the amplitude of A_3 is almost as large as A_0 ($A_0/A_3 \approx 11/10$) whereas for the tripole $A_0/A_2 \approx 7/4$ after $t = 200$. The $\alpha = 7$ vortex used here is unstable to $k = 2$ perturbations, and unstable modes with $k = 2$ get excited by the invariably present numerical noise. As a consequence A_2 also grows. After the triangular vortex has formed, A_2 continues to grow in an oscillatory fashion but it levels off near the value shown at $t = 300$. Also A_4 (not shown) grew to levels similar to those of A_2. We ran a high-resolution simulation (256^2) where we started with the circular component ω_0 at $t = 300$, (shown below in figure 8*b*), and perturbed with the $k = 2$ component at $t = 300$. A rapid growth of a $k = 2$ instability ensued, leading to a breakup into dipoles. Thus, the stability of the triangular vortex is determined by the entire vorticity field, not by the underlying circular component. Carnevale & Kloosterziel (1994) found in fact that the triangular vortex is stable with respect to arbitrary but small perturbations.

Next, in figure 5(*c*), the $A_k(t)$ are shown for the experiment of figure 4 for $k = 0, 4, 8, 12$ and also $A_2(t)$. After the square vortex has formed A_2 continues to grow and around $t = 150$ it equals A_4 in amplitude. At this time the core is no longer square (figure 4*c*). The $k = 2$ component continues to grow, and rapid changes in A_0, A_4 and the other amplitudes ensue. These changes are associated with the events shown in panels (*d*–*f*) of figure 4, i.e. the continued stretching of the core, the merger of the satellites, and the subsequent dipole splitting. Thus, the square vortex is short-lived due to a $k = 2$ instability. In other simulations we subtracted the ω_2-component at $t = 125$. The amplitude A_2 could be brought down to machine precision level $O(10^{-15})$. The resulting square vortex rotated for a while, but noise generated in the numerical scheme due to the finite resolution and round-off errors again led to the growth of a $k = 2$ component, and dipole splitting occurred again. The square vortex is thus unstable to the smallest perturbations.
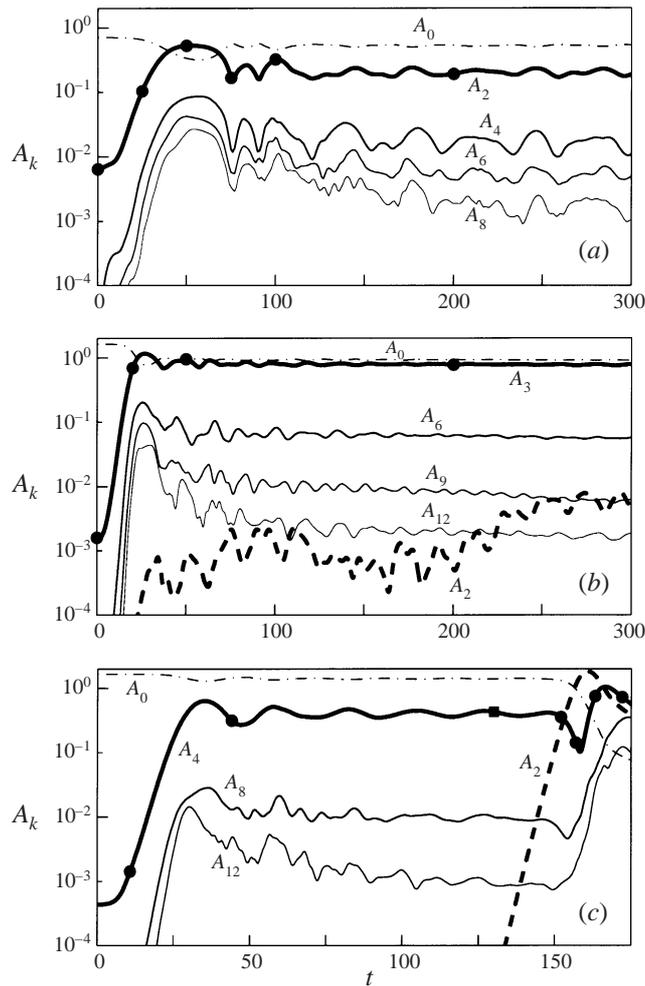
FIGURE 5. Evolution of amplitudes of various azimuthal components ω_k for (*a*) the tripole of figure 2, (*b*) the triangular vortex of figure 3 and (*c*) the square vortex of figure 4. For a definition of A_k see text. Black dots indicate the times at which vorticity distributions were shown in figures 2, 3 and 4.

In what follows *m* will indicate the azimuthal wavenumber associated with each instability. This facilitates the discussion and generalization of the results. The most unstable normal modes for each case are shown in figure 6. These are the ω_m-components for the tripole ($m = 2$), triangular vortex ($m = 3$) and the square vortex ($m = 4$) at early times when the evolution is still dominated by linear dynamics. Figure 6(*a*) showing ω_2 for the tripole compares well with the figure shown by Carton & Legras (1994) who determined the fastest growing normal mode for the $\alpha = 3$ vortex through normal modes analysis. In each example there are 2*m* cells of vorticity of alternate sign surrounded by another 2*m* cells whose centres are rotated with respect to the centres of the inner cells. The radius dividing the inner and outer cells is in each case near the position of the inflection point of $\bar{\omega}_\alpha(r)$, while the maxima of the inner cells are near the zero crossing of $\bar{\omega}_\alpha(r)$.

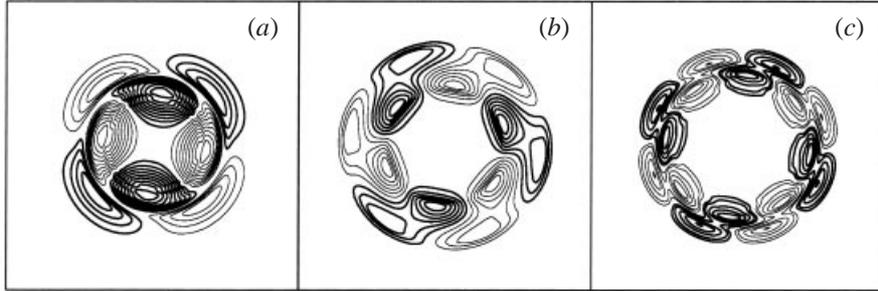In the first row of figure 7 vorticity contours are shown for the three compound

FIGURE 6. Contours of the most unstable modes leading to (*a*) tripole formation in figure 2, (*b*) triangular vortex formation in figure 3 and (*c*) square vortex formation in figure 4. These are the components ω_2, ω_3 and ω_4, respectively, numerically determined at (*a*) $t = 20$, (*b*) $t = 10$ and (*c*) $t = 10$. The ω_m were calculated using (6) and a simple linear interpolation scheme for the azimuthal integral at sufficiently many radial positions. Contour increments are $\Delta\omega = \max(|\omega_m|)/10$ in each panel. Thick lines indicate positive values, thin lines negative values. Box sizes are smaller than figures 2–4 in order to show more details.

vortices. The second row shows contours of the ω_m-component and the third row the ω_{2m}-component (first harmonic). Contour levels are the same in the second and third rows. For the tripole and the triangular vortex the maximum amplitude of ω_{2m} is somewhere between 10% and 20% of the maximum amplitude of ω_m, while for the square vortex the maximum amplitude of ω_{2m} is less than 10% of the maximum of ω_m which is why the last panel is empty. Note the difference between the ω_m patterns shown in figure 6 and in the second row of figure 7. Nonlinear effects have substantially altered them between the time of exponential growth and the time of saturation. In figure 8 we compare the original vorticity distributions that gave rise to the compound vortices with the ω_0-component of the tripole, triangular vortex and square vortex. In the case of the tripole and the triangular vortex (figure 8*a*, *b*) the cores of $\bar{\omega}_{\alpha=3}$ and $\bar{\omega}_{\alpha=7}$, respectively, have lost some of their negative vorticity while the outer annuli of positive vorticity have somewhat broadened and decayed in amplitude. This is the region where the satellites are located. In the case of the square vortex (figure 8*c*) the core vorticity of $\bar{\omega}_{\alpha=7}$ is virtually unaltered.

Because for each case in figure 5, $A_m > A_{2m} > A_{3m} > \cdots$, the question arises as to how many of the azimuthal components ω_k determine the main features of the vorticity distributions during the evolution. Figure 5(*a*) shows that at $t = 50$ the A_k with $k \neq 0$ reach a maximum during the tripole formation. The tripole at $t = 50$ was shown in figure 2(*c*). Figure 9(*a*) shows that $\omega_0 + \omega_2$ is not sufficient. Adding ω_4 we get figure 9(*b*) which still does not capture the main features seen in figure 2(*c*). When we also add ω_6 there is a tendency for the core to become elongated and bend at the tips (figure 9*c*). It improves a little more if we add ω_8 (figure 9*d*). To resolve the thin tendrils of core vorticity which wrap around the satellites in figure 2(*c*), many of the higher azimuthal components need to be added. Next consider the fully formed tripole shown in figure 2(*f*). In figure 9(*e*) we show the approximation $\omega \approx \omega_0 + \omega_2$, in figure 9(*f*) $\omega \approx \omega_0 + \omega_2 + \omega_4$. In the latter case the shape of the core and the satellites compares well with that of the original. Also the positions of maximum amplitude in the satellites coincide. The amplitudes differ by roughly 10%. For $\omega_0 + \omega_2$ the main features of the tripole are also clearly seen in figure 9(*e*), but there are obvious differences between the core shapes. The higher azimuthal harmonics only contribute to the details at this point. Note for example the small ring-like feature at a large
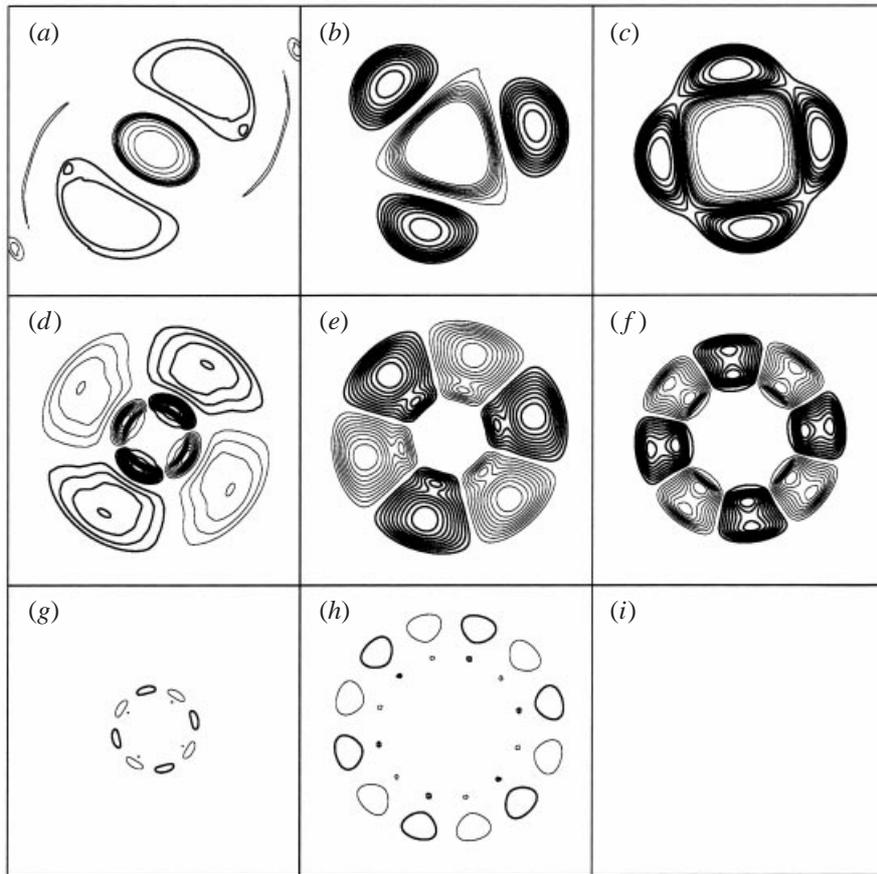
FIGURE 7. Contour plots of vorticity and separate components for the three compound vortices. The first row shows (*a*) the tripole of figure 2*f* at $t = 200$, (*b*) the triangular vortex of figure 3*d* at $t = 200$ and (*c*) the square vortex of figure 4 at $t = 130$ (indicated by a black square in figure 5*c*). The second row shows contours of ω_m for (*d*) the tripole ($m = 2$), (*e*) the triangular vortex ($m = 3$) and (*f*) the square vortex ($m = 4$). Contour increments in the first and second row are $\Delta\omega = \max(|\omega_{(m)}|)/10$. The third row shows contours of ω_{2m} at the same levels as in the second row. Box sizes are the same as in figure 6.
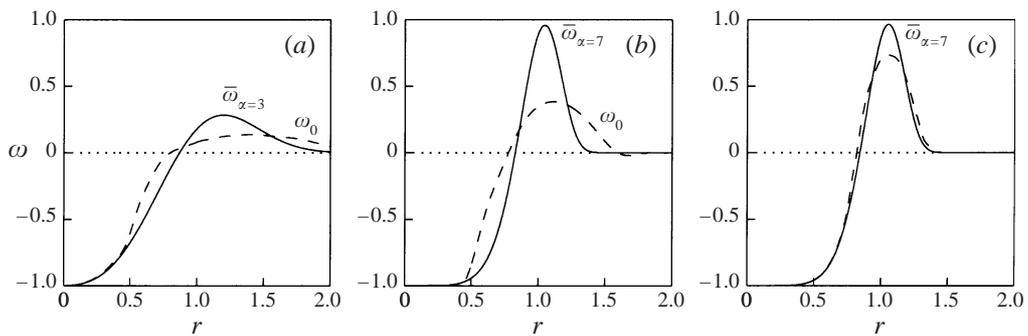

FIGURE 8. (*a*) $\bar{\omega}_{\alpha=3}$ and the ω_0-component (dashed line) of the tripole at $t = 200$, (*b*) $\bar{\omega}_{\alpha=7}$ and the ω_0-component (dashed line) of the triangular vortex at $t = 200$, (*c*) $\bar{\omega}_{\alpha=7}$ and the ω_0-component (dashed line) of the square vortex at $t = 130$.
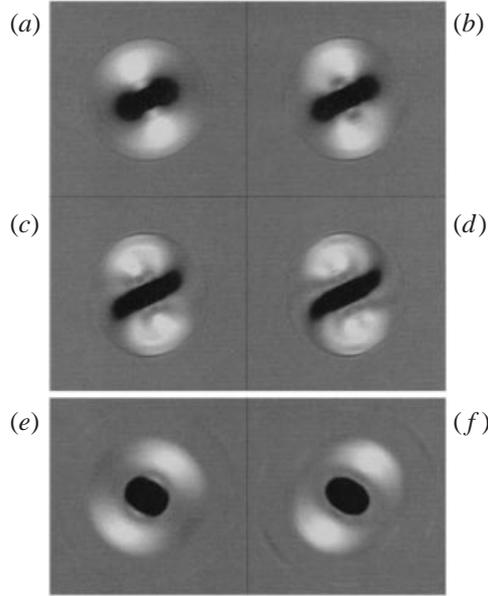
FIGURE 9. The field of figure 2c (tripole at $t = 50$) approximated by (a) $\omega \approx \omega_0 + \omega_2$, (b) $\omega_0 + \omega_2 + \omega_4$, (c) $\omega_0 + \omega_2 + \omega_4 + \omega_6$ and (d) $\omega_0 + \omega_2 + \omega_4 + \omega_6 + \omega_8$. The field of figure 2(f) (tripole at $t = 200$) is approximated in (e) by $\omega \approx \omega_0 + \omega_2$ and (f) $\omega_0 + \omega_2 + \omega_4$. Uniform grey away from the central region indicates zero vorticity, black and darker grey indicate negative vorticity, white and lighter grey indicate positive vorticity.

radius in figure 9(e, f). It is due to the vorticity filaments seen in figure 2(f). Many higher harmonics need to be added to reconstruct such small-scale features. Similarly, for the triangular and square vortex we found that $\omega_0 + \omega_m$, with $m = 3$ and $m = 4$, respectively, captures their main features while at intermediate times when the $A_{k \neq 0}$ peak (see figure 5b, c) the higher harmonics ω_{3m}, ω_{4m} etc. are needed to reconstruct the small-scale filaments which are then present.

3. Low-dimensional dynamical system

Since only a small number of components ω_k dominate during the unfolding of the instabilities, we investigate whether the same is true *dynamically*. That is, we question whether the instabilities and saturation can be described using a small number of azimuthal wavenumbers. The starting point is the two-dimensional inviscid vorticity equation in polar coordinates (Batchelor 1967)

$$\frac{\partial \omega}{\partial t} + \frac{1}{r}\frac{\partial \psi}{\partial \theta}\frac{\partial \omega}{\partial r} - \frac{1}{r}\frac{\partial \psi}{\partial r}\frac{\partial \omega}{\partial \theta} = 0. \tag{8}$$

In this we substitute expansions of the form

$$\psi(r, \theta; t) = \sum_{n=0}^{\infty} \sum_{k=-\infty}^{+\infty} a_n^k(t)\varphi_n^k(r, \theta), \quad \omega(r, \theta; t) = \sum_{n=0}^{\infty} \sum_{k=-\infty}^{+\infty} b_n^k(t)\varphi_n^k(r, \theta), \tag{9}$$

where the φ_n^k are complex and orthonormal: $\int_0^\infty \int_{-\pi}^{+\pi} \varphi_n^k(\varphi_{n'}^{k'})^\star \mathrm{d}\theta r \mathrm{d}r = \delta_{nn'}\delta_{kk'}$ (a $\star$ denotes complex conjugate). Then formally

$$\{a_n^k, b_n^k\} = \langle\{\psi, \omega\}, \varphi_n^k\rangle, \quad \langle f, g\rangle \equiv \int_0^{+\infty} \int_{-\pi}^{+\pi} f g^\star \mathrm{d}\theta r \mathrm{d}r. \tag{10}$$

Through projection (Galerkin method) of (8) on the φ_n^m and elimination of the a_n^k through use of the relation $\omega = -\nabla^2\psi$, a system of coupled ODEs can be derived for the evolution of the vorticity expansion coefficients (see Appendix A):

$$\frac{\mathrm{d}b_r^m}{\mathrm{d}t} + \mathrm{i}\sum_{p=0}\sum_{q=0}\sum_{k+l=m} I\begin{pmatrix} m & k & l \\ r & p & q \end{pmatrix} b_p^k b_q^l = 0. \tag{11}$$

The orthonormal functions are

$$\varphi_n^k(r,\theta) = c_n^k \times (\tfrac{1}{2}r^2)^{|k|/2}\mathrm{e}^{-r^2/4}L_{|k|+n}^{|k|}(\tfrac{1}{2}r^2)\mathrm{e}^{ik\theta}, \quad c_n^k = \left(n!/2\pi(|k|+n)!^3\right)^{1/2}. \tag{12}$$

The L_n^m (with $n \geqslant m$) are associated Laguerre polynomials of order $n-m$, defined as the mth derivative of the ordinary Laguerre polynomial:

$$L_n^m(x) \equiv \frac{\mathrm{d}^m}{\mathrm{d}x^m}L_n(x), \quad L_n(x) \equiv \mathrm{e}^x\frac{\mathrm{d}^n}{\mathrm{d}x^n}x^n\mathrm{e}^{-x}.$$

If $\int\int_{\mathbf{R}^2}\psi^2\mathrm{d}\theta r\mathrm{d}r < \infty$, $\int\int_{\mathbf{R}^2}\omega^2\mathrm{d}\theta r\mathrm{d}r < \infty$, then the expansions (9) are possible, i.e. the set $\{\varphi_n^k\}$ is complete on $\mathbf{R}^2$ in a square-integrable sense (see Higgins 1977). Details about the calculation of the interaction matrix $I\begin{pmatrix} m & k & l \\ r & p & q \end{pmatrix}$ and some of its properties are given in Appendix A. The condition $m = k + l$ in (11) says that components with azimuthal wavenumber m are generated through the nonlinear interaction between wavenumber k and l components. At infinite resolution all $k, l, m \in (-\infty, +\infty)$ and $p, q, r \in [0, +\infty)$ are considered in (11). By truncation at finite limits we obtain a finite-dimensional dynamical system.

When $k = 0$ the φ_n^k have no azimuthal dependence. In figure 10(a) the first three of these circular modes φ_n^0 are shown ($n = 0, 1, 2$). The first ($n = 0$) is proportional to $\exp(-r^2/4)$, the second ($n = 1$) to $(1 - r^2/2)\exp(-r^2/4)$. As n further increases the Laguerre polynomials in (12) make the φ_n^k more oscillatory. In figure 10(b–e) the real part of φ_n^1 and φ_n^2 is shown for radial wavenumbers $n = 0, 1$. The real part of φ_0^1 shown in figure 10(b) is proportional to $r\exp(-r^2/4)\cos\theta$. This changes sign once as θ runs from 0 to 2π. This gives a 'dipole'-like pattern. The graph in figure 10(c) has more 'cells' because φ_1^1 contains the factor $r(r^2 - 4)\exp(-r^2/4)\cos\theta$, which changes sign not only with increasing θ but also with r. Similar remarks apply to the functions with higher azimuthal wavenumbers. In expansions like (9) we get terms $b_n^k\varphi_n^k + b_n^{-k}\varphi_n^{k\star}$ when $k \neq 0$. Since ω is real we have $b_n^{-k} = b_n^{k\star}$. The graphs in figure 10 showing $\mathrm{Re}(\varphi_n^k)$ can thus be viewed as vorticity distributions with two non-zero expansion coefficients $b_n^k = b_n^{-k} = 1/2$, whereas complex $b_n^k = |b_n^k|\mathrm{e}^{-ik\phi}$ rotates the patterns over an angle ϕ. The b_n^0 are always real. The φ_n^k decay rapidly with increasing r and they are well-suited to represent compact vorticity distributions. To illustrate this we show in figure 11 that with a few φ_n^k patterns can be formed that resemble the compound vortices discussed in §2. In each case we used only φ_0^0, φ_1^0 plus φ_0^m ($m = 2$ for tripole pattern, $m = 3$ for triangular pattern, $m = 4$ for square pattern) with appropriate amplitudes (see caption).

In the simulations to be discussed below we integrated (11) forward in time with a fifth-order Runge–Kutta driver with adaptive stepsize control (see Press *et al.* 1989), after assigning initial values to the various expansion coefficients b_p^k. In the truncated model we limit the azimuthal wavenumbers to a finite range so that only φ_n^k with $k \in [-k_{\max}, +k_{\max}]$ are used. For each k in this range we also truncate at finite radial wavenumbers N_k, i.e. only φ_n^k with $n \leqslant N_k$ are used. The truncations are symmetric, i.e. for each k used, $-k$ is also used and $N_{-k} = N_k$. The calculation of
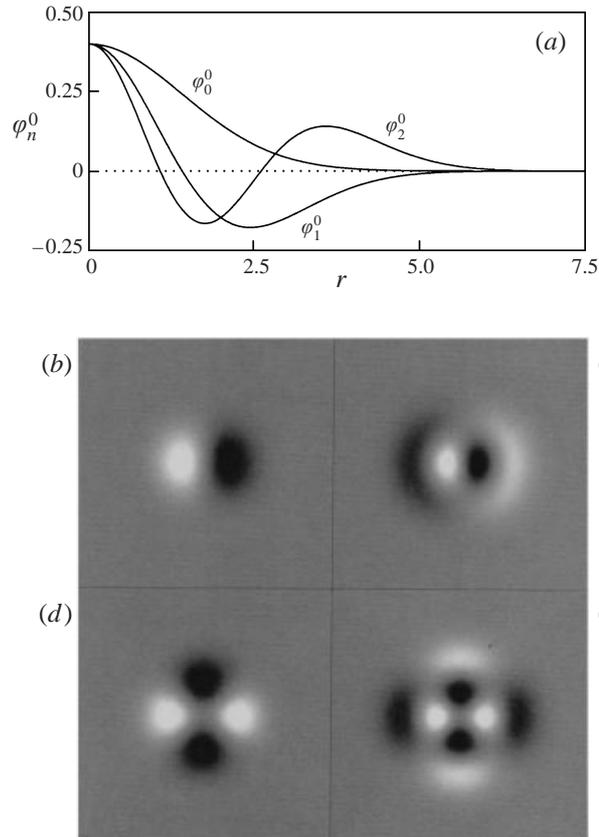
FIGURE 10. (a) The first three circular modes φ_n^0 ($n = 0, 1, 2$), given by (12), as a function of r (distance from origin) and shaded contour plots of the real part of (b) φ_0^1, (c) φ_1^1, (d) φ_0^2 and (e) φ_1^2. Box size is 15×15. The origin of the coordinate system is at the centre of the boxes. Shading is as before.

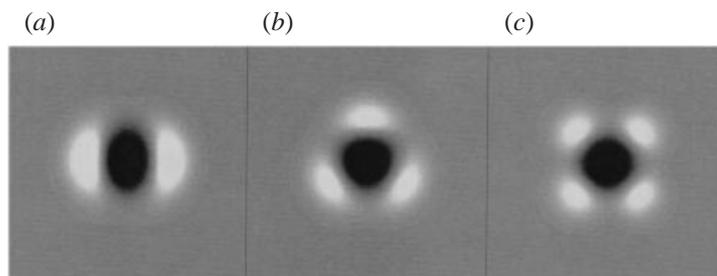FIGURE 11. (a) A tripole, (b) a triangular vortex and (c) a square vortex created with a sum of a few φ_n^k. In each case we took in (9) $b_0^0 = -1, b_1^0 = -1$ and (a) $b_0^2 = 0.4$, (b) $b_0^3 = -0.2$ and (c) $b_0^4 = -0.2$ plus $b_n^{-k} = (b_n^k)^\star$ when $k \neq 0$.

the interaction coefficients is complicated and computationally costly because the φ_n^k are *not* eigenfunctions of the Laplace operator (see Appendix A). For this reason we calculated the coefficients only for radial truncations $N_k < 10$ and a small set of azimuthal wavenumbers.

3.1. *Linear stability*

Next we need to consider what minimal truncations are needed so that the main features of the evolution of instabilities are well modelled. One criterion is that normal modes instability should occur. We will see that this is possible with a relatively small number of the expansion functions. To investigate the linear stability of circular vortices with the truncated model, $\bar{\omega}(r)$ needs to be expressed in terms of the circular modes φ_n^0. We can approximate the vorticity distribution of a vortex by a truncated sum in our expansion functions. In the definition (12) we have written these functions in terms of a non-dimensional radial variable r. By scaling this variable, we can attempt to improve the degree to which any truncated series of the expansion functions will fit the initial vorticity profile. Thus we approximate the initial distribution by

$$\bar{\omega}(r) \approx \bar{\omega}_{N_0}(r;\varepsilon) \equiv \sum_{n=0}^{N_0} \bar{b}_n^0 \varphi_n^0(r/\varepsilon,\theta), \quad \bar{b}_n^0 = \langle \bar{\omega}, \varphi_n^0(r/\varepsilon,\theta) \rangle, \tag{13}$$

where the scaling factor ε is chosen such that for a given radial truncation N_0

$$d(\bar{\omega}, \bar{\omega}_{N_0}) \equiv \int_0^\infty (\bar{\omega}(r) - \bar{\omega}_{N_0}(r;\varepsilon))^2 \mathrm{d}r \tag{14}$$

is minimal. For example, consider the $\alpha = 2$ vortex with vorticity (see (3))

$$\bar{\omega}(r) = (r^2 - 1)\mathrm{e}^{-r^2} = -(\pi/2)^{1/2} \left\{ \varphi_0^0(2r,\theta) + \varphi_1^0(2r,\theta) \right\}.$$

An absolute minimum $d(\bar{\omega}, \bar{\omega}_{N_0}) = 0$ (a perfect fit) is found at $\varepsilon = 1/2$ for any truncation $N_0 \geqslant 1$. In this case $\bar{b}_0^0 = \bar{b}_1^0 = -(\pi/2)^{1/2}$ while all other $\bar{b}_n^0$ with $n > 1$ are zero. For all other α-values in (3) there is no exact fit with a finite sum of scaled the φ_n^0. But, as will be shown, close approximations can be found by minimizing $d(\bar{\omega}, \bar{\omega}_{N_0})$ for sufficiently large N_0.

Perturbations with a given azimuthal wavenumber k are of the form

$$\omega'_{N_k}(r,\theta;t) = \sum_{p=0}^{N_k} b_p^k(t) \varphi_p^k(r/\varepsilon,\theta) + \text{c.c.}, \tag{15}$$

with ε in (15) equal to the one minimizing $d(\bar{\omega}, \bar{\omega}_{N_0})$. The resolution N_k need not be equal to N_0. In the truncated model the initial condition is $\bar{\omega}_{N_0} + \omega'_{N_k}$. Substitution in (11) and discarding terms quadratic in the perturbation expansion coefficients leads to the linearized dynamics

$$\frac{\mathrm{d}b_p^k(t)}{\mathrm{d}t} = \mathrm{i} \sum_{p'=0}^{N_k} \mathrm{M}_{pp'}^k b_{p'}^k(t) \quad \mathrm{M}_{pq}^k = -2 \sum_{r=0}^{N_0} I \begin{pmatrix} k & 0 & k \\ p & r & q \end{pmatrix} \bar{b}_r^0, \quad (p,q = 0,\ldots,N_k). \tag{16}$$

The coefficients $\bar{b}_r^0$ are constants, determined by the optimal approximation $\bar{\omega}_{N_0}$. The factor 2 appears because we used the symmetry property $I\begin{pmatrix} m & k & l \\ r & p & q \end{pmatrix} = I\begin{pmatrix} m & l & k \\ r & q & p \end{pmatrix}$ (see Appendix A). We write (16) as $\dot{\boldsymbol{b}}^k = \mathrm{i}\boldsymbol{M}^k \boldsymbol{b}^k$ (a dot indicates time derivative), where $\boldsymbol{M}^k$ is the $(N_k + 1) \times (N_k + 1)$ real matrix defined above and $\boldsymbol{b}^k(t)$ is the $2(N_k + 1)$-dimensional vector $\boldsymbol{b}^k(t) = (b_0^k(t),\ldots,b_{N_k}^k(t))^{\mathrm{T}}$. The complex expansion coefficients b_p^k (for $k > 0$) count for two because the real and imaginary part are independent. Assuming exponential time-dependence $\boldsymbol{b}^k(t) = \mathrm{e}^{\mathrm{i}\lambda t}\boldsymbol{b}^k$, one gets the matrix eigenvalue problem $\boldsymbol{M}^k \boldsymbol{b}^k = \lambda \boldsymbol{b}^k$. Denoting the eigenvalues by λ_n ($n = 0,\ldots,N_k$) we find that, as

in §2, an eigenvector $\boldsymbol{b}_{(n)}^k$ grows exponentially in the linearized dynamics if $\text{Im}(\lambda_n) < 0$. The evolution of the vorticity perturbation associated with a normal mode is

$$\omega'(r, \theta; t) = e^{i(k\theta + \lambda_n t)} \sum_{p=0}^{N_k} b_{p(n)}^k f_p^k(r/\varepsilon) + \text{c.c.}, \qquad (17)$$

where the $b_{p(n)}^k$ are the components of $\boldsymbol{b}_{(n)}^k$ and f_p^k is φ_p^k as in (12) without the factor $e^{ik\theta}$. Thus, a normal mode with $\text{Re}(\lambda_n) \neq 0$ rotates and grows in amplitude when $\text{Im}(\lambda_n) < 0$.

For the case of tripole formation, we use the initial profile given by $\alpha = 3$ as in the simulation of figure 2. For a given truncation level N_0 for the $k = 0$ modes, we must first determine the best radial scaling ε. The first row in figure 12 shows $d(\bar{\omega}, \bar{\omega}_{N_0})$ as a function of ε for truncations $N_0 = 2, 4$ when $\bar{\omega}$ is the $\alpha = 3$ vortex. This is the vortex which when perturbed gives rise to tripole formation (figure 2). The ε-value at which an absolute minimum is reached is indicated by a dot in each case. In the second row we compare $\bar{\omega}_{N_0}$ corresponding to these minima with $\bar{\omega}_{\alpha=3}$. For $N_0 = 2$ small deviations are seen in figure 12(c). At truncation $N_0 = 4$, $\bar{\omega}_{N_0}$ is indistinguishable from $\bar{\omega}_{\alpha=3}$ (figure 12d). The optimal approximations to $\bar{\omega}_{\alpha=3}$ were subjected to a stability analysis as outlined above. It is supposed to be unstable to $k = 2$ perturbations (see figure 1b). For both resolutions N_0 we determined the most unstable $k = 2$ normal modes with $3 \leqslant N_2 \leqslant 9$. The results are shown in the third row of figure 12. The dashed line indicates the value of 7.67×10^{-2} from figure 1(b), which was calculated at high resolution.

Figure 12(e) shows that for each N_2 the growth rate is systematically too low when $\bar{\omega}_{\alpha=3}$ is resolved with $N_0 = 2$. With the almost perfect match found with $N_0 = 4$ (figure 12d) we see in figure 12(f) that deviations are at most 5% for $6 \leqslant N_2 \leqslant 9$. Figure 12(f) has clear signs of convergence with increasing N_2. At the intermediate resolution $N_0 = 3$ (not shown) the optimal approximation differed somewhat less from $\bar{\omega}_{\alpha=3}$ than for $N_0 = 2$, while the growth rates were scattered about the true value with deviations as large as 30%. The most unstable normal modes for $N_2 = 3, 5, 7, 9$ are depicted in figure 13. The structure extracted from high-resolution numerical calculations was shown in figure 6(a). In figure 13(a, b) the normal modes with $N_2 = 3, 5$, respectively, compare poorly with figure 6(a). Their corresponding growth rates deviate 11% and 8.5%, respectively. For $N_2 = 7, 9$ we see in figure 13(c, d) the characteristic 'tear'-shape of the inner cells also seen in figure 6(a). The growth rates for the latter two deviate 5% and 2% from the true value. No unstable modes were found for radial resolutions $N_2 < 3$. Thus, minimally *four* φ_n^k are needed to resolve unstable modes.

In figure 14 we show results for $\bar{\omega}_{\alpha=7}$. This is the vortex which gives rise to triangular vortex and square vortex formation (figures 3, 4). Figure 14(a) is a graph of $d(\bar{\omega}_{\alpha=7}, \bar{\omega}_{N_0})$ as a function of ε for $N_0 = 9$. The approximation $\bar{\omega}_{N_0}$ for the optimal ε-value is shown in figure 14(b) together with $\bar{\omega}_{\alpha=7}$. Only slight differences are visible. Figure 14(c) gives the growth rates of the most unstable $k = 4$ normal modes with $3 \leqslant N_4 \leqslant 9$. The dashed line indicates the true value of 2.0×10^{-1} from figure 1(b). For resolutions $N_4 = 3, 4$ no unstable modes are found. Thus, in this case at least six φ_n^k are needed to resolve unstable normal modes. For $5 \leqslant N_4 \leqslant 9$ deviations from the true growth rate are at most 13% and about 5% for $N_4 = 8, 9$. The most unstable normal modes with $k = 4$ corresponding to these last two resolutions (not shown) compared well with the filtered ω_4-component shown in figure 6(c). For $N_0 < 9$ the optimal approximation to $\bar{\omega}_{\alpha=7}$ was poorer than in figure 14(a) and the growth rates deviated more than shown in figure 14(c).
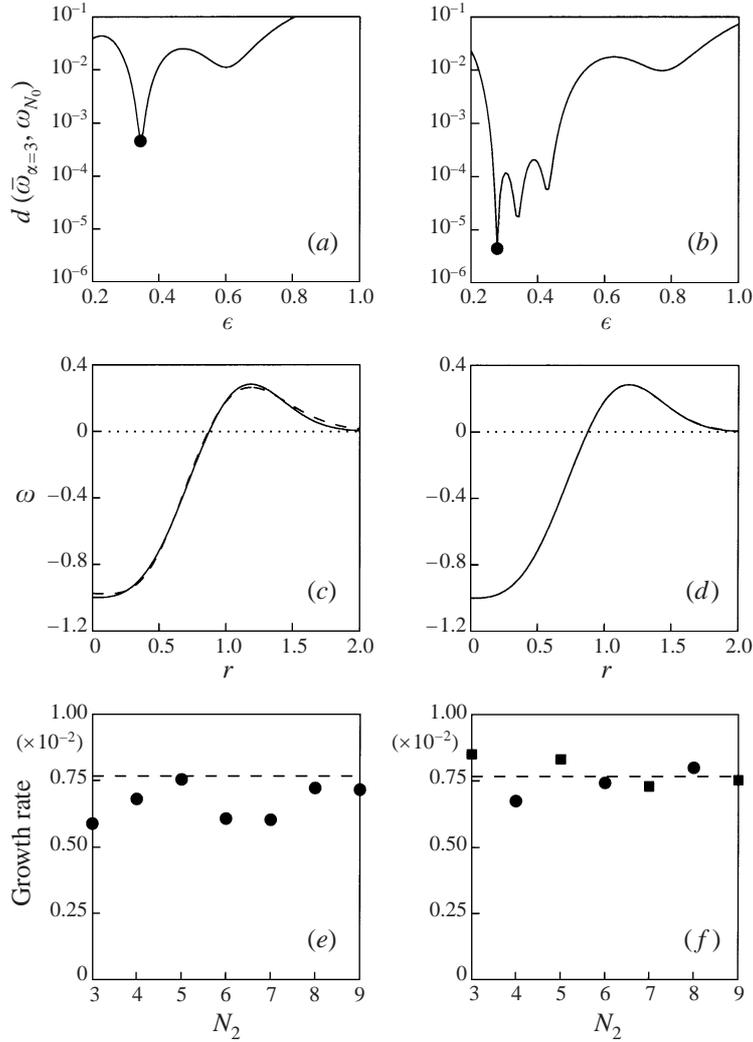
FIGURE 12. (a) $d(\bar\omega_{\alpha=3}, \bar\omega_{N_0})$ given by (14) for $N_0 = 2$ and (b) for $N_0 = 4$, as a function of ε. Absolute minima (best fits) are reached for $N_0 = 2$ at $\varepsilon = 0.344$ and for $N_0 = 4$ at $\varepsilon = 0.280$ (black dots). The second row shows the approximation $\bar\omega_{N_0}$ (dashed line) corresponding to these minima for (c) $N_0 = 2$ and (d) $N_0 = 4$ together with $\bar\omega_{\alpha=3}$ (solid line). The third row shows the growth rates of the most unstable $k = 2$ modes for both approximations with resolutions $3 \leqslant N_2 \leqslant 9$. Squares in panel (f) mark the resolutions for which the normal modes are shown in figure 13.

3.2. *Nonlinear dynamics at low-order truncations*

We have established that at low-order truncations the system can exhibit normal modes growth. Here we determine what dynamically the necessary ingredients are for instabilities to saturate at finite amplitude, with compound vortex formation as a result. For this we integrated (11) forward in time using just a few azimuthal wavenumbers and low radial resolutions. Because according to (12) φ_p^k has a polynomial part of order $r^{2p+|k|}$, a φ_p^l has a higher amplitude at a given large r than φ_p^k when $|l| > |k|$. In order to have the groups of modes with different azimuthal wavenumbers $\{k, l\}$ cover approximately the same area, we used truncations $N_l < N_k$ when $|l| > |k|$.
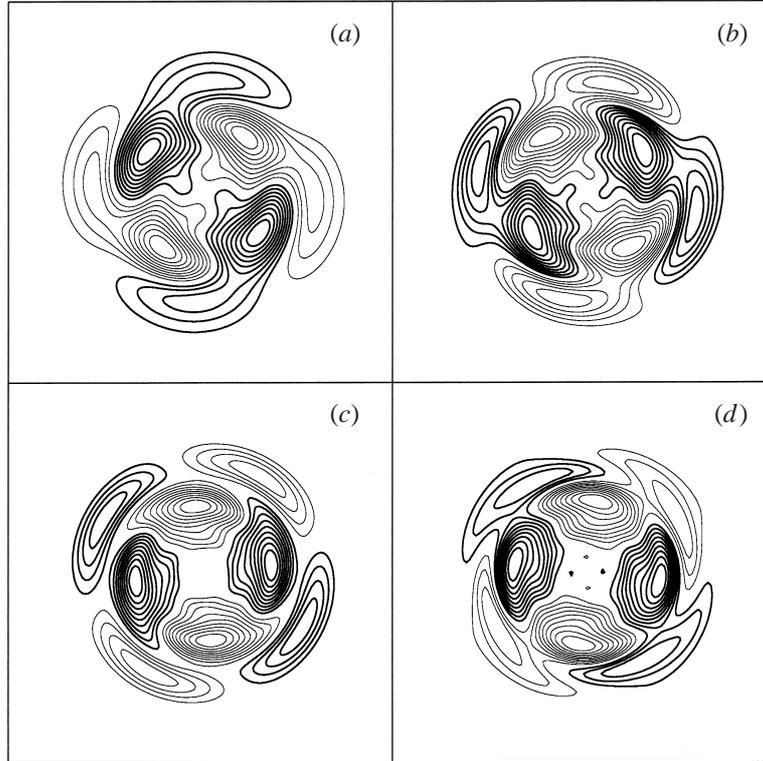
FIGURE 13. Contour plots of the most unstable $k = 2$ normal mode for $\bar{\omega}_{\alpha=3}$ vortex approximated according to (13) with $N_0 = 4$ and $\varepsilon = 0.280$. Resolutions are (a) $N_2 = 3$, (b) $N_2 = 5$, (c) $N_2 = 7$ and (d) $N_2 = 9$. Thick lines indicate positive values, thin lines negative values.

Further, the experiments and analysis of §2 suggest that the basic instability and the saturation at a finite level rely mostly on the presence of the fundamental mode ω_m and its harmonics in addition to the circular mode. The dynamical systems discussed below used for this reason only wavenumbers $k = 0, m, 2m, \dots$. Azimuthal truncations were thus taken at $k = m$, $k = 2m$, etc. None of the intermediate wavenumbers were used; this allows us to focus entirely on the formation process with no consideration of instabilities due to perturbations with azimuthal wavenumbers other than $k = m, 2m, \dots$. In such truncated models the following set of equations determines the dynamics:

$$
\frac{\mathrm{d}b_r^0}{\mathrm{d}t} = -2\mathrm{i}\sum_{p=0}^{N_m}\sum_{q=0}^{N_m} \overbrace{\mathrm{i}I\begin{pmatrix} 0 & m & -m \\ r & p & q \end{pmatrix} \mathrm{Im}\left(b_p^m b_q^{m\star}\right)}^{\text{feedback}} \quad (r = 0,\dots,N_0)
$$

$$
-2\mathrm{i}\underbrace{\sum_{p=0}^{N_{2m}}\sum_{q=0}^{N_{2m}} \mathrm{i}I\begin{pmatrix} 0 & 2m & -2m \\ r & p & q \end{pmatrix} \mathrm{Im}\left(b_p^{2m} b_q^{2m\star}\right)}_{\text{feedback}} - 2\mathrm{i}\sum_{p=0}^{N_{3m}}\sum_{q=0}^{N_{3m}}\underbrace{\{\cdots\}}_{\text{fdbck}} - \cdots \quad (18)
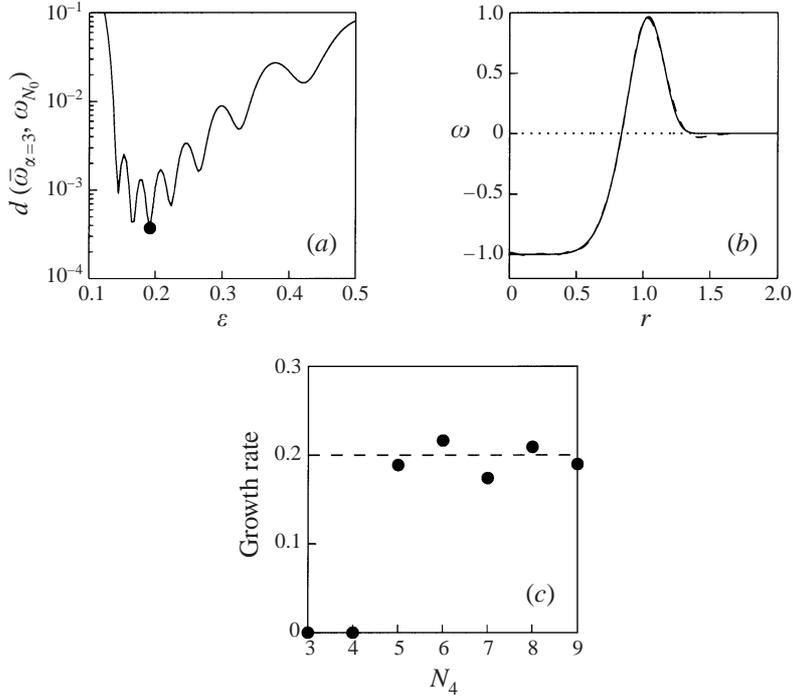$$

FIGURE 14. (*a*) $d(\bar{\omega}_{\alpha=7}, \bar{\omega}_{N_0})$ given by (14) as a function of ε for $N_0 = 9$, (*b*) the approximation $\bar{\omega}_{N_0}$ (dashed line) corresponding to the optimal approximation found with $\varepsilon = 0.192$ and $\bar{\omega}_{\alpha=7}$ (solid line) and (*c*) the growth rates of the most unstable $k = 4$ modes for this approximation with resolutions $3 \leqslant N_4 \leqslant 9$.

$$\frac{\mathrm{d}b_r^m}{\mathrm{d}t} = -2\mathrm{i} \sum_{p=0}^{N_0} \sum_{q=0}^{N_m} \overbrace{I \begin{pmatrix} m & 0 & m \\ r & p & q \end{pmatrix} b_p^0 b_q^m}^{\text{advection}} \quad (r = 0, \ldots, N_m)$$

$$-2\mathrm{i} \underbrace{\sum_{p=0}^{N_m} \sum_{q=0}^{N_{2m}} I \begin{pmatrix} m & -m & 2m \\ r & p & q \end{pmatrix} b_p^{m\star} b_q^{2m}}_{\text{feedback}} -2\mathrm{i} \sum_{p=0}^{N_{2m}} \sum_{q=0}^{N_{3m}} \underbrace{\{\cdots\}}_{\text{fdbck}} - \cdots \quad (19)$$

$$\frac{\mathrm{d}b_r^{2m}}{\mathrm{d}t} = -2\mathrm{i} \sum_{p=0}^{N_0} \sum_{q=0}^{N_{2m}} \overbrace{I \begin{pmatrix} 2m & 0 & 2m \\ r & p & q \end{pmatrix} b_p^0 b_q^{2m}}^{\text{advection}} \quad (r = 0, \ldots, N_{2m})$$

$$-2\mathrm{i} \underbrace{\sum_{p=0}^{N_m} \sum_{q=0}^{N_m} I \begin{pmatrix} 2m & m & m \\ r & p & q \end{pmatrix} b_p^m b_q^m}_{\text{first harmonic generation}} -2\mathrm{i} \sum_{p=0}^{N_{2m}} \sum_{q=0}^{N_{4m}} \underbrace{\{\cdots\}}_{\text{fdbck}} - \cdots \quad (20)$$

and so on. The factors 2 in front of the sums in (19) and (20) are due to the symmetry property (A 7*a*) of the interaction matrix (see Appendix A). To get (18) the anti-symmetry property (A 7*b*) of the interaction matrix and the fact that $b_p^{-k} = b_p^{k\star}$ were combined. The time rate of change of a given mode's amplitude with azimuthal wavenumber m' is determined by nonlinear interactions of modes with wavenumbers

k, l which satisfy $k + l = m'$. For these interactions we use the notation $k + l \rightarrow m'$. Circular mode amplitudes b_r^0 change only due to self-interactions of non-circular modes, i.e. $k + (-k) \rightarrow 0$ with $k \neq 0$. 'Feedbacks' are interactions $k + l \rightarrow m'$ where either $|m'| < |k|$ or $|m'| < |l|$. Any interaction $0 + k \rightarrow k$, which simply represents the advection of the wavenumber k component by the circular component, we shall refer to as 'advection'. The generation of harmonics occurs when both $k, l > 0$ or $k, l < 0$. We obtain the system truncated at azimuthal wavenumber $k = 2m$ and radial truncations N_0, N_m, N_{2m} if the summations that involve $k = 3m, k = 4m, \ldots$ (upper indices $N_{3m}, N_{4m}, \ldots$) are discarded in (18)–(20). We refer to this as the $(0, m, 2m)$ system. If also (20) is discarded plus all terms involving $k = 2m, 3m, \ldots$ in (18) and (19), we get the dynamics for the system truncated at $k = m$ and radial truncations N_0, N_m. This we call the $(0, m)$ system. In Appendix B it is shown that the system conserves enstrophy Q at any truncation, where

$$Q = \sum_{k \geqslant 0} Q_k, \quad Q_0 = \sum_{p=0}^{N_0} |b_p^0|^2, \quad Q_{k>0} = 2 \sum_{p=0}^{N_k} |b_p^k|^2. \tag{21}$$

Thus, in the $(0, m)$ system, $Q_0 + Q_m$ is constant and in the $(0, m, 2m)$ system, $Q_0 + Q_m + Q_{2m}$ is constant.

3.2.1. *The $(0, m)$ system*

The stability analysis in §3.1 showed that for unstable normal modes a certain minimum radial resolution N_m is required. For $\bar{\omega}_{\alpha=3}$ unstable modes with $k = 2$ were only found for $N_2 \geqslant 3$, for $\bar{\omega}_{\alpha=7}$ unstable modes with $k = 4$ only for $N_4 \geqslant 5$ (figures 12 and 14). The simplest system that *may* mimic for example tripole formation thus uses only azimuthal wavenumbers $k = 0, 2$ and must have a radial resolution $N_2 \geqslant 3$. We focus on this case here. We take $N_2 = 3$ and a resolution $N_0 = 4$ which is high enough to closely approximate $\bar{\omega}_{\alpha=3}$ (see figure 12d). The initial conditions for (11) are the b_p^0 determined by the optimal approximation to $\bar{\omega}_{\alpha=3}$ plus a small non-zero b_0^2. This projects on the most unstable mode seen in figure 13(a). Using this as an initial condition we integrated (11) forward in time with the (0,2) truncation set of expansion modes. The phase space spanned by the expansion coefficients has in this case $(N_0 + 1) + 2(N_2 + 1)$ dimensions, i.e. it is 13-dimensional. In figure 15(a) we show the ensuing evolution of $A_k(t) = (Q_k(t))^{1/2}$ ($k = 0, 2$), with Q_k given by (21). This is the direct analogue of the $A_k(t)$ defined in (7). Initial exponential growth of A_2 occurs; as in the high-resolution experiments (see figure 5a). This is due to the advection term in (19). Feedback alters the circular components according to (18), and A_0 decreases in amplitude. Since $A_k = Q_k^{1/2}$, an amplitude increase in one component is accompanied by a decrease in the other because in the (0, 2) system $Q_0 + Q_2$ is constant. No saturation at finite amplitude occurs; instead both A_0 and A_2 oscillate forever. A tripole-like pattern is associated with the maxima in A_2 (figure 15b), and a distorted circular vortex with the minima (figure 15c). Vacillation between these two patterns continued, no matter how long we integrated the system. Inspection showed that at the peaks of A_2 the ω_0-component is significantly different from $\bar{\omega}_{\alpha=3}$ while the ω_2-component has the characteristic shape of a neutrally stable mode, which is quite different from unstable modes like those shown in figure 13 (see §3.3). At the minima we found ω_0 very close to $\bar{\omega}_{\alpha=3}$ while the weak ω_2-component neither resembled a neutrally stable mode nor an unstable mode. In systems with higher radial resolutions N_0, N_2 the system exhibited the same behaviour. The absence of saturation is therefore not due to a poor approximation of the unstable normal
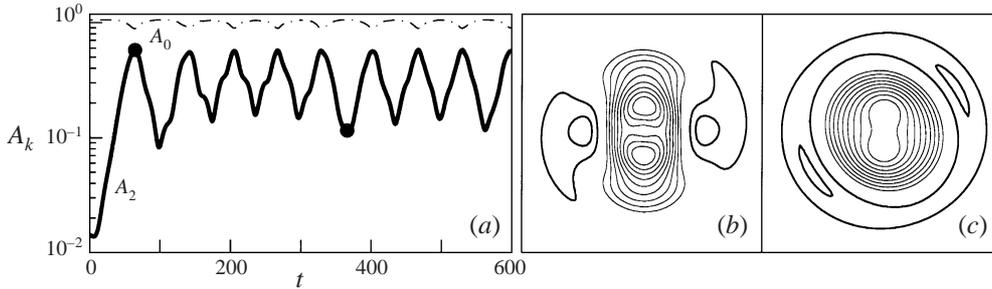
FIGURE 15. (a) Evolution of A_0 and A_2, where $A_k = Q_k^{1/2}$ with Q_k given by (21), after integration of (11) using $k = 0, 2$ and resolutions $N_0 = 4, N_2 = 3$ with as initial condition the b_p^0 for the optimal approximation ω_{N_0} of $\bar{\omega}_{\alpha=3}$ given in figure 12(d), plus a small wavenumber-2 perturbation in the form of a non-zero $b_0^2 = 10^{-2}$, with all other b_p^2 zero. (b) Contours of the resulting field at $t = 65$, (c) the field at $t = 366$. These moments are indicated by black dots in panel (a). Contour increments are $\Delta\omega = \max(|\omega|)/10$, thick contours indicate positive values, thin ones negative values. Box size is 12×12. Total enstrophy $Q = 1.12$.

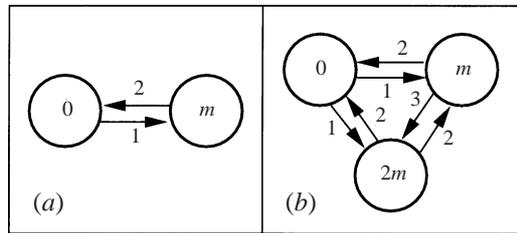FIGURE 16. Schematic diagram of the interactions in minimal systems using (a) wavenumbers $k = 0, m$ and (b) $k = 0, m, 2m$. With reference to equations (18)–(20) $1 =$ advection, $2 =$ feedback, $3 =$ higher-harmonic generation.

mode and the corresponding growth rate. No system using only $k = 0, m$ could either simulate triangular vortex or square vortex formation. Although the phase space is full of periodic orbits (§ 3.3), many of which represent such rotating compound vortices, the dynamics lacks something needed to keep or put the phase flow in the vicinity of such periodic orbits. The dynamics is in these cases a feedback loop as sketched in figure 16(a). It has advection $0 + m \rightarrow m$ and feedback $m + (-m) \rightarrow 0$.

3.2.2. *The* $(0, m, 2m)$ *system*

Next in increasing complexity are systems using $k = 0, m, 2m$. For a study of tripole formation we used the same initial condition as above in the system with radial resolutions $N_0 = 4, N_2 = 3, N_4 = 2$. There are now $2(N_4 + 1)$ additional degrees of freedom and phase space is 19-dimensional. The dynamics is far more complex as is seen in figure 16(b): there are three inter-connected feedback loops. In figure 17(a) we show the evolution of A_0, A_2 and A_4. Again initial exponential growth of A_2 occurs, and A_4, which is initially zero, increases exponentially too. This is due to the higher-harmonic generation in (20). No quasi-periodic behaviour occurs; instead there are irregular oscillations in both A_2 and A_4. As in figure 5(a), A_4 remains at all times smaller than A_2. The amplitude variations in A_2 are smaller than in the simpler dynamics. The six panels in figure 17 show the field at various representative moments. Even at $t = 280$ when A_2 is relatively small the field is clearly tripole-like with pronounced satellites (figure 17g). The simulation was continued far longer
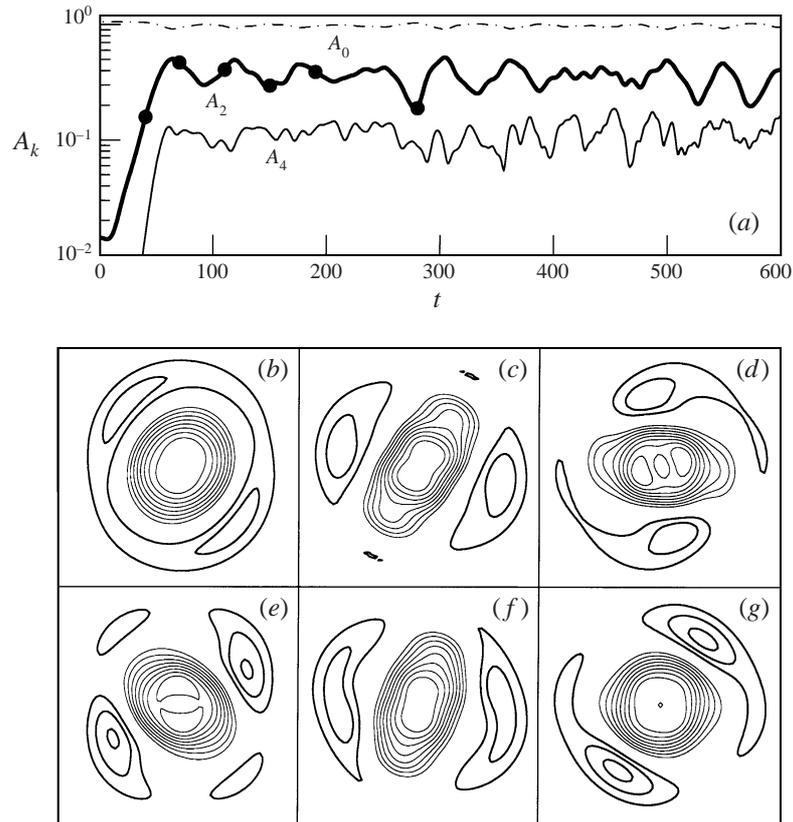
FIGURE 17. (a) Evolution of A_0, A_2 and A_4 after integration of (11) using $k = 0, 2, 4$ and resolutions $N_0 = 4, N_2 = 3, N_4 = 2$ with the same initial condition as for figure 15 and the fields at (b) $t = 40$, (c) $t = 70$, (d) $t = 110$, (e) $t = 150$, (f) $t = 190$ and (g) $t = 280$. Box sizes, contouring and Q are as in figure 15.

than shown. The irregular oscillations continued but at all times the tripole pattern persisted. Between $t = 100$ and $t = 600$ the major axis of the core made 7 turns which is very close to the number of turns the tripole of figure 2 made in that time span.

To determine when and how the ω_4-component affects the dynamics we deleted it from the dynamics at various moments during the evolution and then continued the integration with the system using only $k = 0, 2$. Two examples are shown in figure 18. In the first case we deleted ω_4 from the dynamics at $t = 50$, in the second at $t = 60$. The upper block of panels (a–d) in figure 18 pertains to the first case, the lower block (e–h) to the second. For both cases we show $\omega_0 + \omega_2$ and ω_0 and ω_2 separately as they are at $t = 60$. The difference between the fields is that in the second case ω_4 has been active in the dynamics for an extra time span of $\Delta T = 10$ (between $t = 50$ and $t = 60$). The evolution of A_2 starting at $t = 50$ for the first case is in figure 18(d) (thick line). For comparison A_2 from figure 17(a) in the dynamics including ω_4 is also plotted and A_4 until $t = 50$ (thin lines). The condition at $t = 60$ is such that the ensuing oscillations in A_2 are of the same magnitude as in figure 15(a). The field vacillates between the two extremes seen in figure 15(b, c). In figure 18(h) the evolution of A_2 for the second case is shown, starting at $t = 60$. It now stays

at levels like in figure 17(a). This was also the case when ω_4 was deleted from the dynamics any time after $t = 60$. Again A_2 from figure 17(a) and A_4 until $t = 60$ (thin lines) have been added for comparison. At all times tripole-like fields were found, similar to those in figure 17. The tripole-like fields shown in figure 18(a) and figure 18(e) thus evolve very differently in the dynamics using $k = 0, 2$ after $t = 60$: the one of figure 18(a) returns to almost circular shapes, as in the dynamics that never used ω_4 while the one in figure 18(e) is robust in the dynamics with $k = 0, 2$. Some small differences are apparent between their ω_0- and ω_2-components. The resulting robust tripole of figure 18(e) has larger satellites with centres farther away from the centre and is less asymmetric than the one in figure 18(a). Two conclusions are drawn from this. First, once the tripole in the dynamics with $k = 0, 2, 4$ has formed, the ω_4-component is no longer needed to keep ω_2-amplitudes from dropping to low levels with an accompanying disappearance of the tripole. There is mainly a balance due to the feedback loop between ω_0 and ω_m as sketched in figure 16(a). Secondly, the saturation in the dynamics with $k = 0, 2, 4$ at the levels seen in figure 17(a) is due to the active role of ω_4 in the period prior to the moment the A_2 and A_4 peak for the first time. It brings about small but important changes in ω_0 and ω_2 so that afterwards the tripole persists even when the first harmonic ω_4 is deleted from the dynamics.

Further information concerning the role of ω_4 was obtained by considering various 'mutilations' of the dynamics. One is shown in figure 19(a) where we cut the feedback from the first harmonic to the circular components. This system does not conserve enstrophy. We applied this to the tripole formation process. When running it forward in time we found essentially the same evolution as in the 'uncut' version, i.e. the amplitudes evolved as in figure 17(a) and only after $t = 200$ small deviations became apparent which remained small afterwards. This showed that the feedback $2m + (-2m) \to 0$ is not essential. Another version is shown in figure 19(b) where we also cut the feedback $m + (-m) \to 0$ from the dynamics. In this case the ω_0-component does not change with time, i.e. $\omega_0 = \bar{\omega}_{\alpha=3}$ at all times. Initial exponential growth and saturation of A_2 and A_4 occurred as in figure 17(a) but at higher levels, i.e. with $A_4(t) < A_0 < A_2(t)$ and later, i.e. around $t = 100$ instead of around $t = 60$. Nothing resembling a tripole corresponds to this. But it revealed another essential fact. Had there been no feedback from ω_4 to ω_2, normal modes growth would have continued indefinitely, i.e. the system would have blown up. The feedback changes the ω_2 component from the unstable normal mode form towards that of a neutrally stable mode. The feedback from ω_2 to ω_0 in figure 19(a) has the added effect that ω_0 is changed to forms for which the growth rate of the most unstable mode is smaller and A_0 decreases. For example figure 18(g) shows that in the uncut dynamics ω_0 has a lower maximum at $t = 60$ than initially. Typically such lower amplitudes at the outer inflection point imply lower growth rates of unstable modes. This seems to be the reason for amplitudes to level off earlier with $A_4(t) < A_2(t) < A_0(t)$ when feedback from ω_2 to ω_0 is kept in the dynamics.

The experiments were repeated at various higher resolutions N_2 and N_4. It was found that the minimal model used here is generic and no dramatically different behaviour resulted from using higher resolutions. Well-defined tripoles formed in all cases. Similar results at low-order truncations were obtained for triangle and square vortex formation, i.e. models using just $k = 0, m, 2m$ were sufficient for growth and saturation at the proper levels. Higher radial resolutions were needed because for example for square vortex formation when starting with $\bar{\omega}_{\alpha=7}$ unstable normal modes with $k = 4$ were only found for $N_4 \geqslant 5$ (see §3.1).
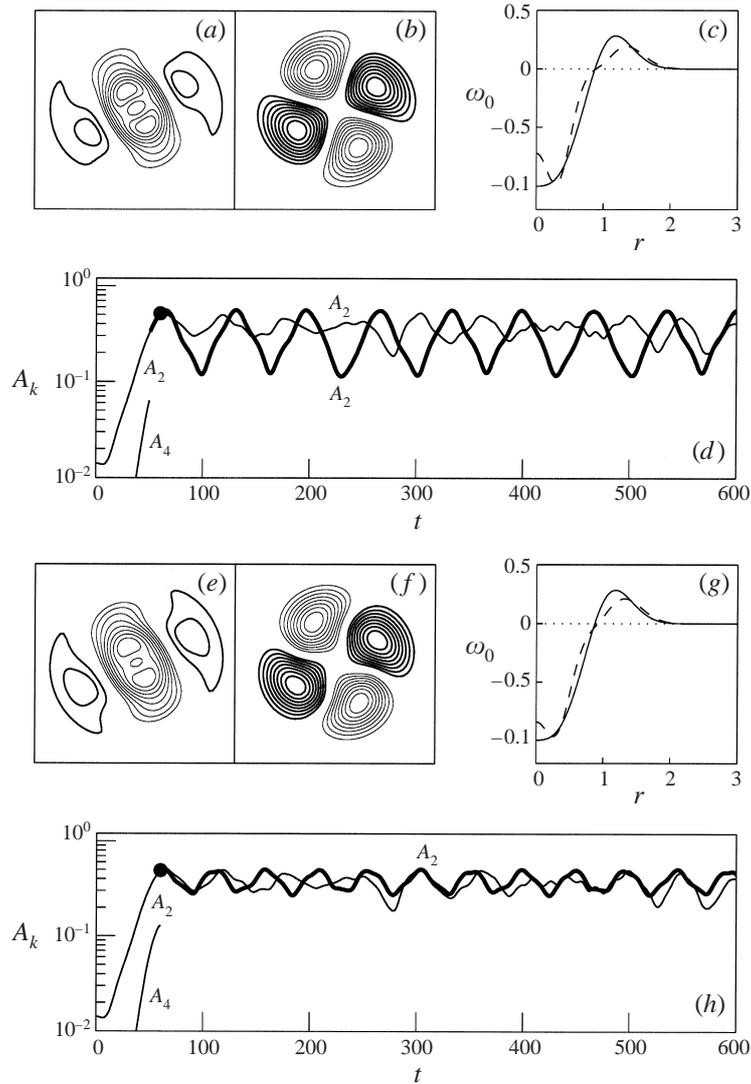
FIGURE 18. Graphs illustrating the consequences of deleting the first-harmonic ω_4 from the dynamics. In the upper block of panels: (a) $\omega = \omega_0 + \omega_2$ at $t = 60$ after deleting ω_4 at $t = 50$, (b) ω_2 for panel (a), (c) ω_0 for panel (a), and (d) the evolution of A_2 (thick line) starting at $t = 50$ in the system using $k = 0, 2$ and truncations $N_0 = 4, N_2 = 3$. Initial evolution is until $t = 50$ as in figure 17. Thin lines show A_2 and A_4 until $t = 50$ from figure 17. In the lower block of panels: (e) $\omega = \omega_0 + \omega_2$ at $t = 60$ after deleting ω_4 at $t = 60$, (f) ω_2 for panel (e), (g) ω_0 for panel (e), and (h) the evolution of A_2 (thick line) starting at $t = 60$. Initial evolution is until $t = 60$ as in figure 17. Thin lines show A_2 and A_4 until $t = 60$ from figure 17.

3.2.3. *Viscous dynamics*

The truncated systems conserve enstrophy which is not realistic for two reasons. First, because in reality during the formation process enstrophy cascades to smaller scales. In the truncated dynamics this transfer stops at the highest radial and azimuthal wavenumbers used, and what would have gone to the smaller scales stays in the system. Secondly, in laboratory and high-resolution experiments there is invariably enstrophy
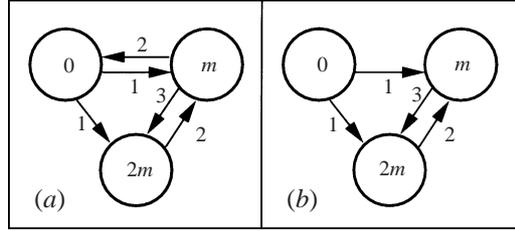
FIGURE 19. Schematic diagram of 'mutilated' dynamics in the system using $k = 0, m, 2m$ used to assess the roles of the feedback (a) $\omega_{2m} + \omega_{-2m} \to \omega_0$ and (b) $\omega_m + \omega_{-m} \to \omega_0$. For conclusions see text. With reference to equations (18)–(20) $1 =$ advection, $2 =$ feedback, $3 =$ higher-harmonic generation.

loss due to viscous effects. To investigate the effects of enstrophy loss in the dynamical system we added Laplacian diffusion to the dynamics, that is, the right-hand side of (8) was put equal to $(1/R)\nabla^2\omega$ where R is a Reynolds number. After projection we obtain the system

$$\frac{\mathrm{d}b_r^m}{\mathrm{d}t} + \mathrm{i}\sum_{p=0}\sum_{q=0}\sum_{k+l=m} I\begin{pmatrix} m & k & l \\ r & p & q \end{pmatrix} b_p^k b_q^l = \frac{1}{R}\sum_{i=r-1}^{i=r+1} \mathrm{L}_{ir}^m b_i^m, \qquad (22)$$

where the coefficients L_{ir}^m are given by (A 2) in Appendix A. If the basis had consisted of eigenfunctions of the Laplace operator, the right-hand side would have had just one term, proportional to b_r^m. In our case we see that diffusion of a given φ_r^m leads also to changes in φ_{r-1}^m and φ_{r+1}^m, i.e. it generates non-zero amplitudes at both a lower and a higher radial wavenumber. We studied tripole formation in the system using $k = 0, 2, 4$ at the same minimal resolutions as before, i.e. $N_0 = 4, N_2 = 3, N_4 = 2$ and the same initial perturbation. An example of the evolution for a Reynolds number $R = 1000$ is shown in figure 20. The amplitudes in figure 20(a) evolve along the same lines as in figure 17(a) until shortly after they first peak. However, after that point the irregular oscillations in the A_k diminish in amplitude while the average value decreases with time. For higher Reynolds numbers the irregular oscillations diminish to the same extent later in time and the decay is slower. The next three panels show the fields at the times indicated by dots in figure 20(a). In contrast to the fields of figure 17, far more symmetric tripoles are found at each instant. In figure 21 we compare projections of the phase trajectories in the inviscid and the viscous dynamics. The projections are on the three-dimensional subspace spanned by b_0^0, $\mathrm{Re}(b_0^2)$ and $\mathrm{Im}(b_0^2)$. In the inviscid dynamics (figure 21a) the trajectory is seen to spiral outwards from the horizontal axis and then to wander around chaotically. With diffusion the trajectory in figure 21(b) is smooth. The loops correspond to rotation of the tripole. The inviscid trajectory lies on a surface of constant Q, given by (21). The projection of this hypersurface fills the interior of the ellipsoid $|b_0^0|^2 + 2|b_0^2|^2 = Q$ in the three-dimensional subspace used in figure 21. The trajectory in figure 21(a) is at all times within this region. The trajectory in figure 21(b) cuts surfaces of progressively smaller $Q(t)$. Here $|b_0^0|$ and $|b_0^2|$ eventually decrease monotonically with time due to the overall enstrophy decay.

We took the fields shown in figure 20 as an initial condition for the inviscid dynamics (11) and integrated it forward. In each case amplitudes were scaled so that the total enstrophy Q was the same and equal to the Q-value of the inviscid experiment of figure 17. The evolution of the A_k in a time span $\Delta T = 600$ is shown
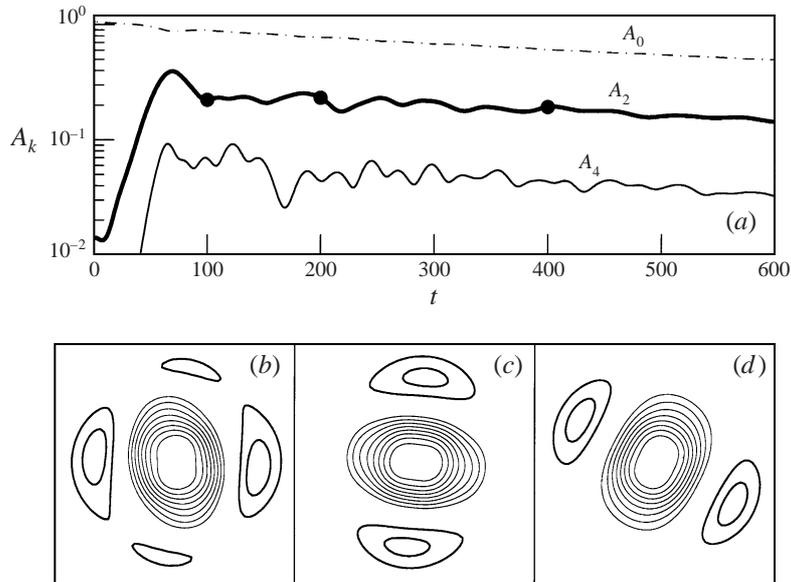
FIGURE 20. (*a*) Evolution of A_0, A_2 and A_4 after integration of (22) with $R = 1000$ using $k = 0, 2, 4$, resolutions $N_0 = 4, N_2 = 3, N_4 = 2$ and with the same initial condition as for figures 15, 17 and the fields at (*b*) $t = 100$, (*c*) $t = 200$ and (*d*) $t = 400$. Box sizes and contouring are as in figures 15 and 17.
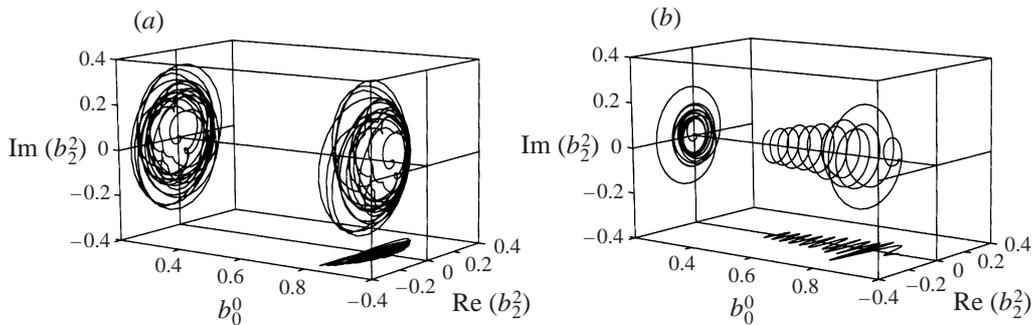

FIGURE 21. Projections of the phase trajectory on the three-dimensional sub-space spanned by b_0^0, $\mathrm{Re}(b_0^2)$ and $\mathrm{Im}(b_0^2)$ for (*a*) the inviscid dynamics of figure 17 and (*b*) the viscous dynamics of figure 20. Total time is for both $\Delta T = 600$.

in figure 22 with to the left the fields from figure 20 that served as initial conditions. It is seen that the ones taken at later times from the viscous experiment lead to smaller amplitude variations with time. In each case the tripole fields of figure 22(*a–c*) persisted with progressively smaller shape variations and rotated between roughly six to eight times in the given time span. The fastest rotation occurred for the tripole of figure 22(*a*), the slowest for the one of figure 22(*c*). Thus, as we take tripoles from the viscous experiment at later times, we get closer to steadily rotating solutions for the inviscid dynamics. In fact, the thin lines drawn in figure 22(*a–c*) are the A_k levels of a stable, steadily rotating solution shown in figure 22(*d*). It was found by taking the field from the viscous simulation at $t = 800$ as an initial condition for a numerical search of nearby periodic solutions to (18)–(20), as described in detail in §3.3. It was already very nearly steady in the inviscid dynamics, i.e amplitude variations were even

smaller than in figure 22(c) for the field at $t = 400$. At $t = 800$ the amplitudes A_k decayed virtually in lockstep at equal ratios. Figure 20(a) shows that at $t = 600$ this is already quite nearly the case. In concise notation periodic solutions in the $(0, m, 2m)$ system are written as $b^0 + b^m e^{im\Omega t} + b^{2m} e^{i2m\Omega t}$, where the vectors b^k are spanned by fixed expansion coefficients b_p^k ($p = 0, 1, \ldots, N_k$). Here Ω is the angular velocity of the rotating pattern. This can be scaled with an arbitrary amplitude γ and more generally solutions are then $\gamma \left(b^0 + b^m e^{im\gamma\Omega t} + b^{2m} e^{i2m\gamma\Omega t} \right)$. Without loss of generality we can put $Q = \gamma^2$. What we find is that in the viscous dynamics with increasing time the phase trajectory gets closer and closer to an orbit determined by fixed b^0, b^m, b^{2m}, Ω and an amplitude γ for which $Q(t) = \gamma^2$. That is, asymptotically the dynamics converges to a solution $(Q(t))^{1/2}(b^0 + b^m e^{im(Q(t))^{1/2}\Omega t} + b^{2m} e^{i2m(Q(t))^{1/2}\Omega t})$. The rate of rotation is at each instant effectively $\Omega' = (Q(t))^{1/2}\Omega$. With the decay of Q there is an associated slow-down and with increasing time it takes longer for the orbit in figure 21(b) to complete a loop. The existence of such solutions to (22) is not obvious *a priori*, neither do we know how to predict b^0, b^m, b^{2m} and Ω. The attraction to a particular tripole of fixed structure was noted by Orlandi & van Heijst (1992) who ran high-resolution simulations with Laplacian diffusion and found that besides the overall amplitude decay at large times the tripole was characterized by a fixed vorticity–streamfunction relation.

3.3. *Periodic orbits*

The experiments discussed in §2 suggest that steadily rotating compound vortices of the tripole, triangular and square vortex kind exist in the absence of any dissipation. In infinite-dimensional phase space they correspond to time-periodic orbits for which

$$\frac{\mathrm{d}b_p^0(t)}{\mathrm{d}t} = 0, \quad b_p^k(t) = |b_p^k|e^{ik(\Omega t + \phi_p^k)} \quad (k = m, 2m, 3m, \ldots),$$
$$b_p^k = 0 \quad (k \neq m, 2m, 3m, \ldots), \tag{23}$$

where m is the fundamental wavenumber characterizing the compound vortex, Ω the angular velocity and ϕ_p^k some as of yet unknown phases. In a truncated model such a solution must satisfy the equations that follow by putting $\dot{b}_r^0 = 0, \dot{b}_r^m = im\Omega b_r^m, \dot{b}_r^{2m} = i2m\Omega b_r^{2m}$ etc. on the left-hand sides of (18)–(20) (a dot indicates time derivative). We will show that both the $(0, m)$ and the $(0, m, 2m)$ system have many of such periodic solutions.

3.3.1. *The $(0, m)$ system*

The simplest system that may have periodic orbits uses only azimuthal wavenumbers $k = 0, m$. If we substitute $\dot{b}_r^m = im\Omega b_r^m$ on the left-hand side of equation (19), it reduces to the linear eigenvalue problem studied in §3.1:

$$m\Omega b_r^m = \sum_{q=0}^{N_m} M_{rq}^m b_q^m, \quad M_{rq}^m = -\sum_{p=0}^{N_0} 2I \begin{pmatrix} m & 0 & m \\ r & p & q \end{pmatrix} b_p^0 \quad (r, q = 0, \ldots, N_m),$$

i.e. it is of the form $M^m b^m = \lambda b^m$ when we put $\lambda = m\Omega$ and b^m is the $2(N_m + 1)$-dimensional vector on the right-hand side of the postulated form $b^m(t) = e^{i\lambda t} b^m$. Therefore it appears that periodic orbits exist if there are neutrally stable normal modes, that is, if among the $N_m + 1$ eigenvalues there are real λ_n. But, the feedback to the circular modes has to be zero because it has tacitly been assumed that the b_p^0 are constants, i.e. in (18) on the left $\dot{b}_r^0 = 0$. This is true because the eigenvectors corresponding to real λ_n are real too. Indicating the components of the eigenvector
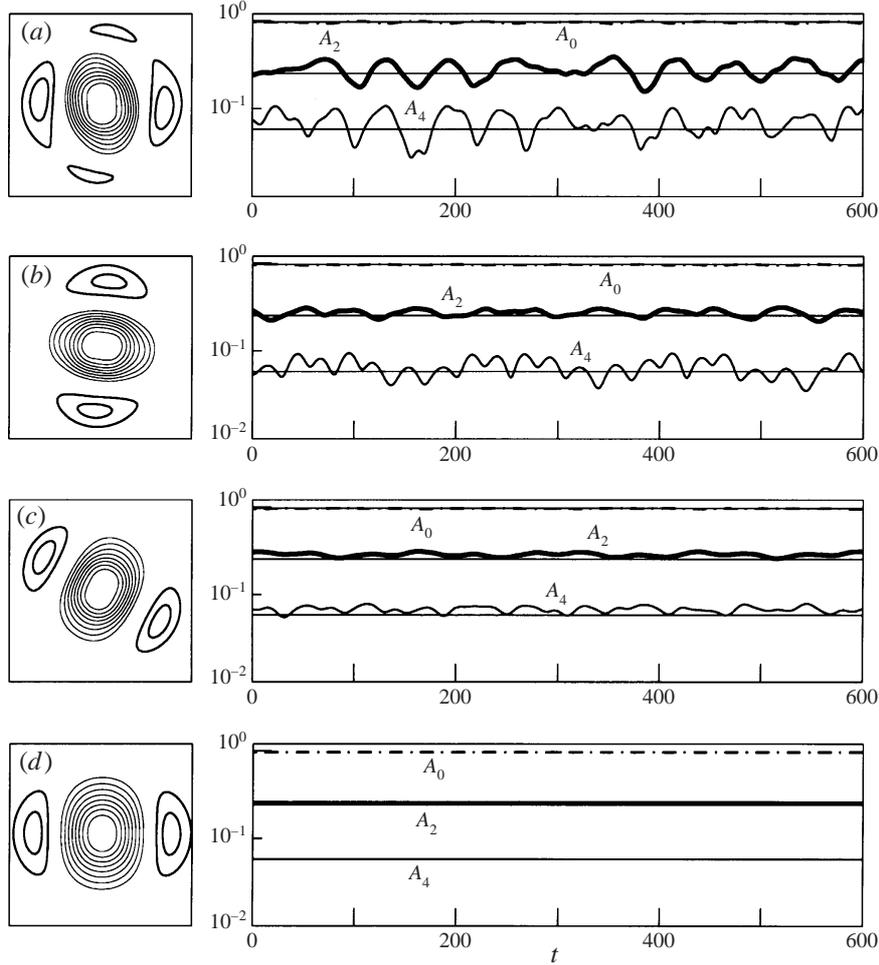
FIGURE 22. Evolution of A_0, A_2 and A_4 $(A_k = Q_k^{1/2})$ after integration of (11) using $k = 0, 2, 4$, resolutions $N_0 = 4, N_2 = 3, N_4 = 2$ and as initial condition (a) the field from the viscous simulation at $t = 100$, (b) the field from the viscous simulation at $t = 200$, (c) the field from the viscous simulation at $t = 400$, each shown in figure 20, after scaling amplitudes such that $Q = 1.12$ as in the inviscid simulation of figure 17. Thin horizontal lines indicate the A_k-levels ($k = 0, 2, 4$) for the field shown in panel (d) which is a steadily rotating stable solution of (11). For more details see text.

$\boldsymbol{b}^m_{(n)}$ by $b^m_{p\,(n)}$, solutions to (19) have therefore components

$$b^m_p(t) = |b^m_{p\,(n)}|\mathrm{e}^{\mathrm{i}m(\Omega_n t + s^m_p \pi/m)}, \quad \Omega_n = \lambda_n/m \quad (p = 0,\dots,N_m), \tag{24}$$

where $s^m_p = 0$ if $b^m_{p\,(n)}$ is positive, and $s^m_p = -1$ when negative. Since $b^m_p b^{m\star}_q = \mathrm{e}^{\mathrm{i}(s^m_p - s^m_q)\pi}$ we have $\mathrm{Im}\left(b^m_p b^{m\star}_q\right) = 0$ for any $\{p, q\}$ and (18) is satisfied. Solutions are written as $\boldsymbol{b}^0 + \beta\boldsymbol{b}^m_{(n)}\mathrm{e}^{\mathrm{i}m\Omega_n t}$ where $\boldsymbol{b}^0 = (b^0_0,\dots,b^0_{N_0})^{\mathrm{T}}$, $\boldsymbol{b}^m_{(n)}$ is as before and β is any constant. Also $\gamma\left(\boldsymbol{b}^0 + \beta\boldsymbol{b}^m_{(n)}\mathrm{e}^{\mathrm{i}m\gamma\Omega_n t}\right)$ is a solution for any real constant γ. Each neutrally stable mode thus generates a two-parameter continuum of periodic orbits.

3.3.2. *The $(0, m, 2m)$ system*

There is no obvious recipe for establishing the existence of periodic solutions when more azimuthal wavenumbers are included. If we take for example a system with $k = 0, m, 2m$ then feedback to the circular components is zero when both $\mathrm{Im}\left(b_p^m b_q^{m\star}\right) = 0$ and $\mathrm{Im}\left(b_p^{2m} b_q^{2m\star}\right) = 0$ for all $\{p, q\}$. Inspection of (18)–(20) reveals that necessarily

$$b_p^m(t) = |b_p^m| \mathrm{e}^{\mathrm{i}m(\Omega t + s_p^m \pi/m)}, \quad b_q^{2m}(t) = |b_q^{2m}| \mathrm{e}^{\mathrm{i}2m(\Omega t + s_q^{2m} \pi/2m)}$$

$$(p = 0, \ldots, N_m)\ (q = 0, \ldots, N_{2m}),$$

with again $s_p^m, s_q^{2m} \in \{-1, 0\}$. This guarantees that the b_r^0 are constant in time, but the remaining problem is no longer linear. By writing $b_r^m = x_r^m + \mathrm{i}y_r^m$ (x_r^m, y_r^m real) and $y_r^0 = 0$, substitution in (18)–(20), setting the left-hand sides equal to $\dot{b}_r^0 = 0$, $\dot{b}_r^m = \mathrm{i}m\Omega b_r^m, \dot{b}_r^{2m} = \mathrm{i}2m\Omega b_r^{2m}$, respectively, and separating the equations into real and imaginary parts, the problem becomes that of solving a set of N coupled nonlinear equations in $N + 1$ real variables

$$F_n(x_0^0, \ldots, x_{N_0}^0; x_0^m, y_0^m, \ldots, x_{N_m}^m, y_{N_m}^m; x_0^{2m}, y_0^{2m}, \ldots, x_{N_{2m}}^{2m}, y_{N_{2m}}^{2m}; \Omega) = 0$$

$$(n = 1, \ldots, N), \quad (25)$$

where $N = (N_0 + 1) + 2(N_m + 1) + 2(N_{2m} + 1)$. The number of variables is $N + 1$ because Ω is also an unknown. Solutions to (25) were numerically determined with the commercially available MATLAB optimization toolbox which utilizes an implementation of a Gauss–Newton method and a Levenberg–Marguardt method. It requires an initial start value for the variables. We searched for periodic orbits on a surface of constant entropy $Q = c$ given by (21). This prevents the search from converging to the zero solution $\{b_p^k = 0, \Omega = 0\}$. Because we have no proof of the existence of periodic orbits and (25) will only be satisfied to an imposed finite degree of precision, the solutions were tested for steadiness by time-integration of (11). In one case we used the tripole of figure 11(*a*) as an initial guess in a system using $k = 0, 2, 4$ and truncations $N_0 = 4, N_2 = 3, N_4 = 2$. It has $\{b_0^0 = -1, b_1^0 = -1, b_0^2 = 0.4\}$. This is not a steadily-rotating solution because according to (20) $k = 4$ components will be generated (first harmonic), feedback occurs which alters the circular components according to (18), and so on. A choice for a start value for Ω was guided by the following. Simulations integrating (11) forward in time, with the (0,2,4) truncation set of expansion modes, showed that the pattern of figure 11(*a*), with the core of negative relative vorticity, tends to rotate in a clockwise direction. This corresponds to $\Omega > 0$. Thus a positive value was assigned to Ω. For negative Ω the search converged to a trivial steady state of circular flow, i.e $\Omega = 0$ and all $b_p^k = 0$ for $k \neq 0$. Given these start values the tripole shown in figure 23(*a*) was found to provide a solution to (25). Contour increments were chosen smaller for positive ω than for negative ω in order to provide a clearer picture of the shape of the satellites. Using this as an initial condition we integrated (11) forward in time for the (0,2,4) truncation set of expansion modes. In figure 23(*b*) we show the ensuing evolution of $A_k(t) = (Q_k(t))^{1/2}$ ($k = 0, 2, 4$) with Q_k given by (21). The A_k and each $|b_p^k|$ were constant to the fourth significant digit, so it is not exactly steady but very nearly so. That the solution rotates becomes clear by plotting it at a later time, as in figure 23(*c*). In the time-span $\Delta T = 500$ the tripole has made $14_{7/8}$ clockwise turns. The rate of rotation was also constant to the fourth significant digit. Even smaller variations in the amplitudes with time could be obtained
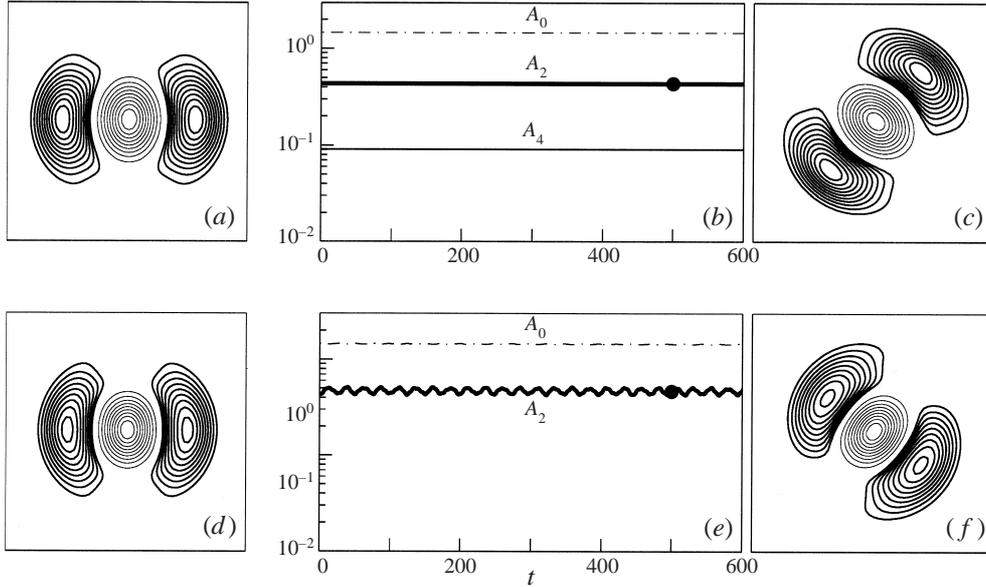
FIGURE 23. (a) Contours of a solution to (25) with resolutions $N_0 = 4, N_2 = 3, N_4 = 3$, (b) evolution of $A_k = Q_k^{1/2}$ when integrating (11) forward in time using $k = 0, 2, 4$ with the above resolutions and the field of panel (a) as initial condition, (c) contours of the resulting field at $t = 500$. (d) the field of panel (a) minus the ω_4-component, (e) evolution of A_k using $k = 0, 2$ in (11) and the field of panel (d) as initial condition, (e) the result at $t = 500$. Box size is 12×12, total enstrophy $Q = 2.32$. Thick contours indicate positive values, thin lines negative values. Contour increments in the cores (negative vorticity) are $\Delta\omega = \max(|\omega|)/10$, for the satellites $\Delta\omega = \max(|\omega|)/25$. For details see text.

by imposing higher degrees of accuracy in the numerical search. In extremely long time integrations no significant amplitude changes occurred which indicates that we are close to a periodic solution that is Lyapunov *stable* to small random perturbations with wavenumbers $k = 0, m, 2m$. This was further verified with simulations where we perturbed the periodic solution and then integrated (11). Significant oscillations in the $A_k(t)$ occurred when the tripole was appreciably distorted but there were no dramatic changes in the pattern with time. Moreover, the amplitude of the oscillations could be controlled by the amplitude of the perturbation.

In figure 23(b) we have $A_2/A_4 \approx 9/2$ and the ω_4-component is thus much weaker than the ω_2-component. When deleting the ω_4-component (all $b_p^4 = 0$) we obtain figure 23(d). Comparison with figure 23(a) shows that only very slight changes result. We used this as an initial condition in the truncated model using wavenumbers $k = 0, 2$ which was then integrated forward in time (again with $N_0 = 4, N_2 = 3$). Small oscillations in A_0, A_2 are seen in figure 23(e). After $\Delta T = 500$ the pattern has made $15 1/4$ clockwise turns (figure 23f). Thus it seems that we are close to a periodic solution in the dynamics using only $k = 0, 2$. In view of the theory discussed above for any $(0, m)$ system, it is concluded that the ω_2-component of the steadily rotating tripole in the $(0, 2, 4)$ system must be close to one of the neutrally stable modes of the circular flow ω_0 generated by the b_p^0 of the tripole shown in figure 23(a). The ω_2-component is shown in figure 24(b). Figure 24(a) has the tripole of figure 23(a) again but with equal contour increments. For the ω_0-component of the tripole and a resolution $N_2 = 3$ we found the four neutrally stable normal modes shown in the next
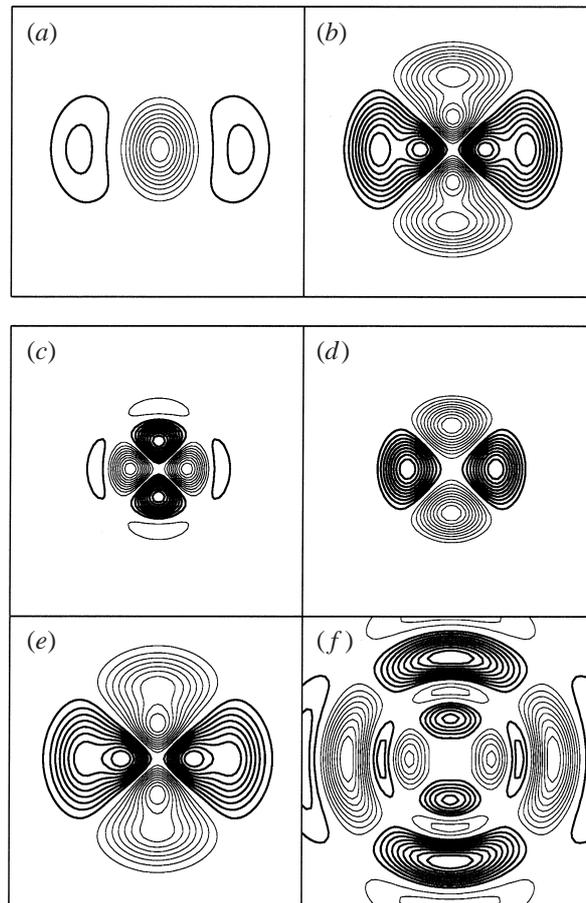
FIGURE 24. (*a*) Same as figure 23(*a*) with equal contour increments $\Delta\omega = \max(|\omega|)/10$, (*b*) the ω_2-component with contour increments $\Delta\omega = \max(|\omega_2|)/10$, and (*c*)–(*f*) contours of the four neutrally stable normal modes at resolution $N_2 = 3$ for the axisymmetric component ω_0 of the field of panel (*a*). Eigenvalues are (*c*) $\lambda = 1.24$, (*d*) 0.570, (*e*) 0.312 and (*f*) 0.133. Box sizes are 12×12. Thick contours indicate positive values, thin lines negative values. For details see text.

four panels of figure 24. Clearly the mode in figure 24(*e*) is close to the ω_2-component. The rate of rotation of the tripole of figure 23(*a*) was $\Omega \approx 0.150$ radians per time unit in the system using $k = 0, 2, 4$. For the mode shown in figure 24(*e*) the eigenvalue is $\lambda \approx 0.312$. With (24) this corresponds to $\Omega = \lambda/2 \approx 0.156$ radians per time unit.

From this it is inferred that for a compound vortex which rotates at a rate Ω in the truncated dynamics using $k = 0, m, 2m$ the following holds: if the ω_{2m}-component is much weaker than the ω_m-component, then ω_m is close to a neutrally stable mode with a corresponding eigenvalue λ for which $\lambda/m \approx \Omega$. If in systems using more azimuthal wavenumbers the components ω_{3m}, ω_{4m} etc. are all much weaker too than ω_m, the above will most likely still be true. This was tested on the triangular vortex of figure 3. Its vorticity contours and that of the $\omega_{3,6}$-components at $t = 200$ were shown in figure 7. Figure 5(*b*) indicates that at this time the triangular vortex is rotating with little change in shape. An optimal approximation ω_{N_0} to its circular component ω_0 (shown in figure 8*b*) was as in §3.1 found by minimizing $d(\omega_0, \bar{\omega}_{N_0})$ given by (14). For $N_0 = 9$, ω_0 could be approximated as closely as shown in figure 14 for the $\alpha = 7$
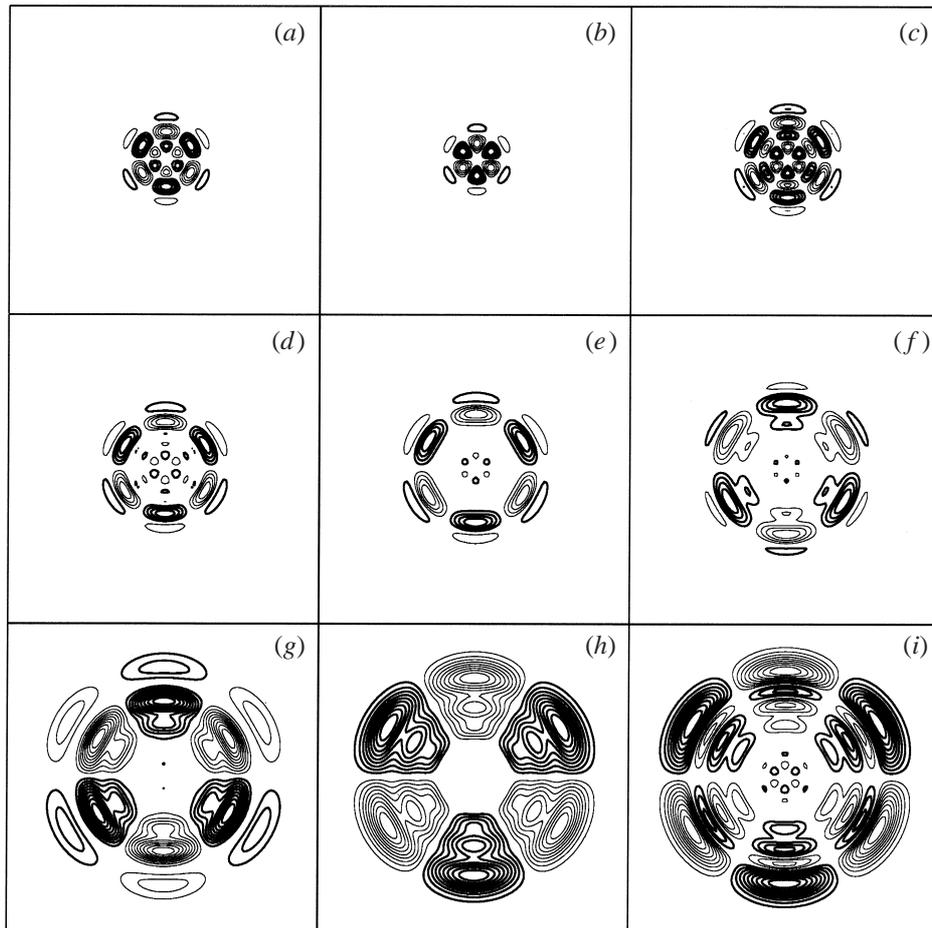
FIGURE 25. Nine neutrally stable modes for the ω_0-component of the triangular vortex at $t = 200$ shown in figure 8(b). The eigenvalue problem was solved with a resolution $N_3 = 8$. Eigenvalues are (a) $\lambda = 1.503$, (b) 1.497, (c) 1.423, (d) 1.195, (e) 0.949, (f) 0.650, (g) 0.405, (h) 0.270 and (i) 0.206. Box sizes are as in figures 6 and 7.

vortex. With the resulting b_p^0 amplitudes we performed the linear stability analysis with an azimuthal resolution $N_3 = 8$. No unstable modes were found, and there were thus 9 neutrally stable modes which are shown in figure 25. Obviously the mode in figure 25(h) is close to the ω_3-component shown in figure 7(e). Similarly, normal modes analysis showed that the ω_4-component of the square vortex in figure 7(f) is close to one of the neutrally stable modes for the ω_0-component of the square vortex. The ω_2-component of the tripole at $t = 200$ in figure 7(d) did not closely resemble one of the neutrally stable modes for ω_0 at this time. The reason appears to be that at $t = 200$ the tripole in the high-resolution experiment is farther from equilibrium than the other two compound vortices.

By taking different initial conditions in a search for solutions to (25) many different periodic solutions were found. An interesting example is shown in figure 26(a) in the system using $k = 0, 2, 4$ and the same radial truncations as above. It has a slightly higher peak vorticity in the satellites and a more elongated core than the previous one of figure 23(a). The difference between the tripoles of figures 23(a) and 26(a) is
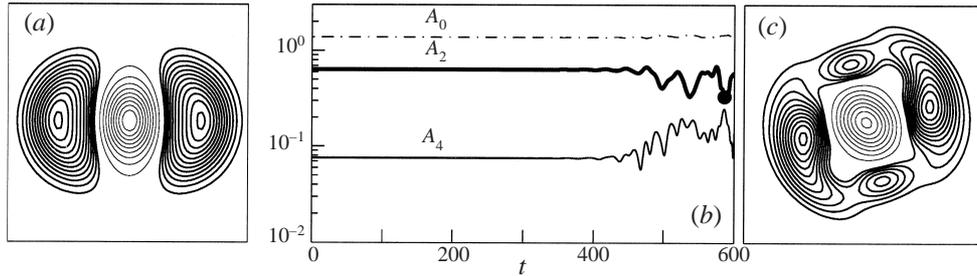
FIGURE 26. (*a*) Contours of a solution to (25) with resolutions $N_0 = 4, N_2 = 3, N_4 = 3$, (*b*) evolution of $A_k = Q_k^{1/2}$ when integrating (11) forward in time using $k = 0, 2, 4$ with the above resolutions and the field of panel (*a*) as initial condition, (*c*) contours of the resulting field at $t = 585$. Box sizes, contouring and Q are as in figure 23.

that in the latter the ω_2-component is somewhat stronger with respect to the ω_0-component (measured by A_2 and A_0) while the ω_4-component is weaker as measured against the ω_2-component. The ω_2-component of the tripole in figure 26(*a*) is like the one shown in figure 24(*b*). The stability behaviour is quite different though. Around $t = 400$ the tripole has made about 12 turns and oscillations appear in the amplitudes A_k (figure 26*b*) which rapidly increase. Figure 26(*c*) shows the field at $t = 585$. This is clearly an unstable periodic solution, i.e. the small errors due to the finite precision of the numerical solution amplify in time. In this case too we deleted the ω_4-component (all $b_p^4 = 0$). We used this as an initial condition in the truncated model using only azimuthal wavenumbers $k = 0, 2$ as above. Small oscillations in A_0, A_2 occured as in figure 23(*h*), but there was no instability in very long time integrations. Also for various basic flows spanned by different $\boldsymbol{b}^0$ and associated neutrally stable modes $\boldsymbol{b}_{(n)}^m$ we checked the stability of the solutions $\boldsymbol{b}^0 + \beta \boldsymbol{b}_{(n)}^m e^{im\Omega_n t}$ in large ranges of amplitudes β, and no instability was found. Thus the dynamics with only $k = 0, 2$ is too severely truncated to capture instabilities of rotating non-circular vortices. The model tripoles of figures 23(*a*) and 26(*a*) were also used as initial conditions for searches in an enlarged system with $k = 0, 2, 4, 6$ and radial truncation $N_6 = 2$. The resulting solutions to (25) were virtually indistinguishable from the solutions in the lower-dimensional system. That is, the search converged to a nearby solution with almost unaltered $\omega_{0,2,4}$ and an additional ω_6-component with smaller amplitude than the ω_4-component. The stability behaviour was the same, i.e. the tripole of figure 23(*a*) when embedded in the enlarged phase space is stable while the tripole of figure 26(*a*) is unstable. Rotation rates changed a mere few percent. Model compound vortices of the triangular and square type were also easily found. In systems using $k = 0, m$ they were as predicted by the theory and stable.

4. Summary and discussion

This study of compound vortex formation had two distinct parts. In the first part (§2) we analysed data from high-resolution numerical experiments showing three different compound vortices emerging from unstable isolated vortices. Tripole formation is the most robust phenomenon (figure 2), triangular and square vortices can only be created under carefully controlled circumstances (figures 3, 4). The square vortex is unstable to infinitesimal perturbations in numerical experiments where the smallest numerical noise is sufficient to destroy it. The modal analysis of §2.2 showed

that all three are the result of similar evolutions. Normal modes growth is followed by the generation of higher harmonics and the formation is completed when nonlinear effects halt the growth and amplitudes level off. Amplitudes A_k of the azimuthal components ω_k have the same ordering $A_0 > A_m > A_{2m} > \cdots$ after formation (figure 5) where for the tripole $m = 2$, for the triangular vortex $m = 3,\ldots$. The most unstable normal modes (figure 6) were obtained by extracting the ω_m-component from the data at early times during the evolution. The splitting of the square vortex ($m = 4$) into dipoles was identified as due to the growth of an $m = 2$ component. The main features of the compound vortices are well-captured by the approximation $\omega \approx \omega_0 + \omega_m$. Prior to equilibration more azimuthal components are needed to reconstruct the existing small-scale filaments, which are particularly prominent in the case of the tripole (figure 9). Our resolution of 256^2 resolved these well. In experiments (not shown) with resolutions 64^2 and 128^2 essentially the same tripole formed, rotating at about the same rate. Thin vorticity filaments are not resolved with such low resolutions. They are thus dynamically of little importance and the higher azimuthal components $\omega_{3m}, \omega_{4m}, \ldots$ therefore appeared to play also dynamically a minor role in the adjustment process.

With this in mind we explored the possibility of reducing the dynamics to as simple as possible a system, that is, a system employing the smallest possible number of azimuthal components ω_k. In §3 a dynamical system was derived by projection of the vorticity equation on the functions (12). These have previously been used by McCalpin (1987) to analyse data from numerical simulations of azimuthally perturbed vortices. For practical reasons the interaction coefficients were computed only for small ranges of azimuthal and radial wavenumbers. In §3.1 we performed linear stability analysis within the dynamical system context. For two cases we showed what minimal number of expansion coefficients need to be kept in the system in order for it to have normal modes instability. This sets a lowest bound for the truncations. Throughout §3 we went as 'low as one can go'. In §3.2 we integrated (11) with severe truncations. Our findings were illustrated through the tripole formation process. The simplest system which uses only $k = 0, m$ could mimic normal modes growth, but not saturation with tripole formation as a consequence. Only when also $k = 2m$ was included in the dynamics did saturation occur. Substantial amplitude variations occurred with time, but never to the extent that the field lost its clear tripole character (figure 17). From experiments where the first harmonic ω_{2m} was deleted from the dynamics at various times it was concluded that it is crucial only during a brief period prior to the moment of saturation. In this period ω_{2m} albeit small in amplitude brings about small but important changes in the ω_0 and ω_m components. After saturation ω_{2m} is no longer needed in the dynamics, i.e. from then onward the tripole persists in the system using only $k = 0, m$ (figure 18). It was further established that the direct feedback $\omega_{2m} + \omega_{-2m} \rightarrow \omega_0$ is unimportant at all times. The feedback loop $\omega_{2m} + \omega_{-m} \rightarrow \omega_m$ plus $\omega_m + \omega_m \rightarrow \omega_{2m}$ takes the initial unstable normal modes form of ω_m to that of a neutrally stable mode. Feedback $\omega_m + \omega_{-m} \rightarrow \omega_0$ changes ω_0 to forms for which the growth rate of unstable normal modes in the linearized dynamics become smaller.

Finally we explored the consequences of allowing enstrophy to escape from the system through the use of Laplacian diffusion. Saturation with far smaller shape vacillations resulted, as in the high-resolution numerical experiments (figure 20). Asymptotically the flow converged to a particular tripole with an accompanying uniform amplitude decay (figure 22). Thus, the main conclusion is that the simplest dynamics that can capture the formation of the compound vortices is that which employs azimuthal wavenumbers $k = 0, m, 2m$. No tendrils like those seen in figure 2(c)

were resolved by the system; for that higher azimuthal wavenumbers are needed (with high radial truncations). But, despite the lack of this feature, tripole formation occurred in the system. The pattern formation process is thus mainly determined by the large scales in the system. Finally, in §3.3 we established the existence of time-periodic solutions in the dynamical system and found that time-periodic solutions in the $(0, m)$ system correspond to compound vortices for which ω_m is a neutrally stable normal mode for the axisymmetric component ω_0. Because typically amplitudes of the higher harmonics ω_{2m}, ω_{3m}, ... are much smaller than for ω_m we speculated that for systems employing more azimuthal wavenumbers this would still approximately hold. This was affirmed by two examples (figures 24 and 25).

The number of degrees of freedom in minimal systems for compound vortex formation using only $k = 0$, m, $2m$ is still quite high. With the truncations $N_0 = 4$, $N_2 = 3$, $N_4 = 2$ for tripole formation for example, phase space is 19-dimensional. It may be possible to simplify the dynamics further by switching to projections on functions that are more closely related to, say, the dominant components of the compound vortices. That is, we could for example instead of using the φ_p^m, use the normal modes for either the initial axisymmetric vortex or the final axisymmetric component. By Gram–Schmidt orthogonalization we can then create a new set of orthonormal functions $\varphi_p'^m$, and similarly for the circular modes and the $k = 2m$ functions. This is of course similar to 'after the fact' EOF-analysis, but it may lead to the discovery of a truly low-dimensional description of the formation process that is amenable to analysis with the tools of dynamical systems theory. As it is, phase flows are very complex and hard to understand. The phase space has an infinity of periodic orbits, some of which are stable, others are unstable (§3.3). In the inviscid dynamics the phase flow wanders chaotically through regions where many nearby periodic orbits reside, but is never asymptotically attracted to one in particular. There can be no domains of attraction surrounding any of the periodic orbits. This is because the inviscid system is time-reversible, i.e. the equations are invariant under sign changes of vorticity and time. Thus, if there were an attracting orbit which corresponds to, say, a clockwise rotating tripole, then there is another orbit corresponding to an anti-clockwise rotating tripole, with the same structure, which is unstable. Two tripoles with the same structure cannot have different stability properties, and this proves the absence of asymptotically attracting periodic orbits. With dissipation added there is an attracting surface, i.e. the flow is not reversible and asymptotically converges to a surface generated by the closed curve $\gamma \left(\boldsymbol{b}^0 + \boldsymbol{b}^m \mathrm{e}^{\mathrm{i}m\phi} + \boldsymbol{b}^{2m} \mathrm{e}^{\mathrm{i}2m\phi} \right)$, where $0 \leqslant \phi \leqslant 2\pi/m$.

In phase-space the 'plane' spanned by all possible vectors $\boldsymbol{b}^0$ represents an infinity of axisymmetric vortices. The subspace spanned by non-zero vectors $\boldsymbol{b}^m$, $\boldsymbol{b}^{2m}$ can be viewed as being perpendicular to this plane. For certain $\boldsymbol{b}^0$-values a point that initially lies slightly off this plane (the initially perturbed vortex) stays close to the plane (stable vortices) or rapidly moves away (unstable vortices). The cases we have discussed correspond to initial positions on the $\boldsymbol{b}^0$-plane with nearby trajectories that lead into a region full of periodic orbits and stay there. There are also points on the $\boldsymbol{b}^0$-plane such that a small perturbation sets off a phase flow on a trajectory that does spend some time near periodic orbits, but eventually leaves it for good and non-periodic flow ensues. The square vortex formation is an example of the latter: first the flow settles near a periodic orbit (square vortex forms) but then dipole splitting occurs, i.e. the trajectory leaves the vicinity of the periodic orbit. Carton & Legras (1994) mention that for $\alpha > 3.2$ in (3) tripoles form which are unstable and split up into dipoles. This is another example of such a scenario.

Some remaining enigmatic questions pertain to the stability of compound vortices, which in phase space is the question of stability of periodic orbits. In the system using $k = 0$, m, $2m$ we found a stable tripole (figure 23a) and an unstable tripole (figure 26a). Stability is used in the sense of Lyapunov here, not asymptotic stability. We just showed that there can be no region surrounding an orbit such that the flow starting at any point within this region converges to the orbit. As mentioned in §3.3 shape vacillations of the perturbed tripole of figure 23(a) could be controlled by the size of the perturbation, but at no time did these oscillations die out with an accompanying return to the original unperturbed tripole. That is, in phase space the flow that starts near this orbit stays near it but does not get attracted to it. Also when time was reversed in (11) the oscillations stayed small but did not tend to zero. In other words, this orbit is surrounded by a region no trajectories escape from, but they also do not converge to the orbit. The tripole of figure 26(a) when used as an initial condition for (11) with time *reversed* ultimately went through similar dramatic shape changes as shown in figure 26(c). Certain trajectories can thus come in from far and stay close to this orbit for a long time but not forever. Other unstable orbits were found when searching for square vortex solutions to (25). When we added to such solutions a small $k = 2$ perturbation in truncated systems using $k = 0$, 2, 4 they were in each case unstable, i.e. the ω_2-component rapidly amplifies as in the high-resolution experiment (figure 4). Thus, there are intrinsically unstable orbits, and orbits with a domain of stability around them. How to discern between them is an open question. In the inviscid dynamics we have as of yet one known conserved quadratic quantity, the enstrophy Q. If other invariants are eventually proven to exist, it may be possible to investigate the stability of periodic orbits with energy methods, that is, to show that stable orbits are local extrema for some linear combination of conserved quantities expressed in the expansion coefficients (see Kloosterziel & Carnevale 1992 for such an approach to the stability question of isolated circular vortices and more recently Davidson 1998 for stability of forced two-dimensional flows).

Appendix A. Calculation of interaction coefficients

When we project the vorticity equation (8) on φ_r^m, and use (9), we obtain

$$\frac{\mathrm{d}b_r^m}{\mathrm{d}t} + \mathrm{i}\sum_{p=0}\sum_{q=0}\sum_{k+l=m} J\begin{pmatrix} m & k & l \\ r & p & q \end{pmatrix} a_p^k b_q^l = 0,$$

$$J\begin{pmatrix} m & k & l \\ r & p & q \end{pmatrix} = \left\langle l\varphi_q^l \frac{\partial \varphi_p^k}{r\partial r} - k\varphi_p^k \frac{\partial \varphi_q^l}{r\partial r}, \varphi_r^m \right\rangle. \qquad (\mathrm{A}\,1)$$

The streamfunction expansion coefficients a_p^k are next expressed in terms of the vorticity expansion coefficients b_n^k using $\omega = -\nabla^2\psi$. The following relation holds:

$$\nabla^2 \varphi_n^k = \tfrac{1}{4}r^2 \varphi_n^k - (2n + 1 + |k|)\varphi_n^k.$$

Thus, the φ_n^k are *not* eigenfunctions of the Laplace operator. For the Laplace operator we write $\nabla^2 \varphi_n^k = \sum_i \mathrm{L}_{in}^k \varphi_i^k$. The lower indices run from $i, n = 0$ to $i, n = +\infty$. It is

found that

$$L^k_{mn} = -\tfrac{1}{2}m^{1/2}(m+|k|)^{1/2} \qquad\qquad (n = m-1)$$

$$= -\tfrac{1}{2}(2m+1+|k|) \qquad\qquad (n = m)$$

$$= -\tfrac{1}{2}(m+1)^{1/2}(m+1+|k|)^{1/2} \quad (n = m+1)$$

$$0 \qquad\qquad\qquad\qquad (\text{all other } n). \qquad (A\,2)$$

Introducing the inverse $(L^k_{mn})^{-1}$, defined by $\sum_p (L^k_{ip})^{-1}L^k_{pj} = \delta_{ij}$, the coefficients a^k_n and b^k_n are related according to

$$b^k_m = -\sum_n L^k_{mn}a^k_n, \quad a^k_n = -\sum_m (L^k_{nm})^{-1}b^k_m, \qquad (A\,3)$$

which is the spectral equivalent of the relation $\omega = -\nabla^2\psi$ and its inverse. Using (A 3) in (A 1) we arrive at (11) with

$$I\begin{pmatrix} m & k & l \\ r & p & q \end{pmatrix} = \tfrac{1}{2}\sum_{p'}(L^k_{p'p})^{-1}J\begin{pmatrix} m & k & l \\ r & p' & q \end{pmatrix} + \tfrac{1}{2}\sum_{q'}(L^l_{q'q})^{-1}J\begin{pmatrix} m & l & k \\ r & q' & p \end{pmatrix}. \qquad (A\,4)$$

With some effort it is found that

$$J\begin{pmatrix} m & k & l \\ r & p & q \end{pmatrix} = \tfrac{1}{2}(k-l)A\begin{pmatrix} m & k & l \\ r & p & q \end{pmatrix} + \tfrac{1}{2}(|k|l - k|l|)B\begin{pmatrix} m & k & l \\ r & p & q \end{pmatrix}$$

$$+ lC\begin{pmatrix} m & l & k \\ r & q & p \end{pmatrix} - kC\begin{pmatrix} m & k & l \\ r & p & q \end{pmatrix} \qquad (A\,5)$$

where

$$A\begin{pmatrix} m & k & l \\ r & p & q \end{pmatrix} = 2\pi c^k_p c^l_q c^m_r \int_0^\infty x^{(|k|+|l|+|m|)/2}e^{-3x/2}L^{|k|}_{|k|+p}L^{|l|}_{|l|+q}L^{|m|}_{|m|+r}(x)\mathrm{d}x,$$

$$B\begin{pmatrix} m & k & l \\ r & p & q \end{pmatrix} = 2\pi c^k_p c^l_q c^m_r \int_0^\infty x^{(|k|+|l|+|m|)/2-1}e^{-3x/2}L^{|k|}_{|k|+p}L^{|l|}_{|l|+q}L^{|m|}_{|m|+r}(x)\mathrm{d}x, \quad \Big\} \quad (A\,6)$$

$$C\begin{pmatrix} m & k & l \\ r & p & q \end{pmatrix} = 2\pi c^k_p c^l_q c^m_r \int_0^\infty x^{(|k|+|l|+|m|)/2}e^{-3x/2}L^{|k|}_{|k|+p}L^{|l|+1}_{|l|+q}L^{|m|}_{|m|+r}(x)\mathrm{d}x,$$

with the constraint $m = k+l$. The normalization constants c^k_p are given by (12). These integrals have exact solutions in the form of a sum of algebraic expressions (details are available upon request from the authors). We wrote a computer program which calculates these algebraic terms, thus providing us with the values of the J in (A 4). One can only sum over a finite number of terms in (A 4), and the question arises whether (A 4) converges for a particular combination of indices, assuming we have the inverse Laplacian to sufficient accuracy. We used large N for the Laplace matrices (10^4 or more) to calculate the inverse, and summed until a fractional accuracy of 10^{-4} was obtained for each coefficient $I\big(\begin{smallmatrix} m & k & l \\ r & p & q \end{smallmatrix}\big)$. The N were varied as needed such that the results became insensitive to any further increases in N. To determine a coefficient we have in general to sum a large number of integrals (A 6) which makes

the calculation computationally costly. Some properties are:

$$I\begin{pmatrix} m & k & l \\ r & p & q \end{pmatrix} = I\begin{pmatrix} m & l & k \\ r & q & p \end{pmatrix}, \quad I\begin{pmatrix} m & k & l \\ r & p & q \end{pmatrix} = -I\begin{pmatrix} -m & -l & -k \\ r & q & p \end{pmatrix},$$

$$I\begin{pmatrix} m & k & l \\ r & p & q \end{pmatrix} = I\begin{pmatrix} k & m & -l \\ p & r & q \end{pmatrix} + I\begin{pmatrix} l & m & -k \\ q & r & p \end{pmatrix}.$$

(A 7a,b,c)

The symmetry and anti-symmetry properties (A 7a, b) are established by close inspection of (11), (A 4) and (A 5). It follows that $I\begin{pmatrix} 0 & k & -k \\ r & p & p \end{pmatrix} = 0$, i.e. there is no feedback to the circular components due to nonlinear interactions of a particular mode with itself. Also $I\begin{pmatrix} 0 & 0 & 0 \\ r & p & q \end{pmatrix} = 0$, which expresses that two circular modes do not interact, i.e. an inviscid circularly symmetric flow is stationary. In Appendix B we show that (A 7c) follows from enstrophy conservation in the fully resolved inviscid dynamics.

If the φ_p^k *were* eigenfunctions of the Laplace operator, i.e. $\nabla^2 \varphi_p^k = -\lambda^2(p,k)\varphi_p^k$, then $a_p^k = b_p^k/\lambda^2(p,k)$. The interaction coefficients (A 4) would then have been

$$I'\begin{pmatrix} m & k & l \\ r & p & q \end{pmatrix} = \tfrac{1}{2}J'\begin{pmatrix} m & k & l \\ r & p & q \end{pmatrix} / \lambda^2(p,k) + \tfrac{1}{2}J'\begin{pmatrix} m & l & k \\ r & q & p \end{pmatrix} / \lambda^2(q,l),$$

where the primes indicate the case with Laplacian eigenfunctions for the expansion. Computationally this is a much simpler case. All previous studies of the barotropic vorticity equation we are aware of fall into this class (some are cited in Appendix B).

Appendix B. Enstrophy conservation at any truncation

Lorenz (1960) noticed the property of enstrophy conservation at any truncation in his study of the barotropic vorticity equation on a doubly periodic domain by direct inspection of the interaction coefficients, for which he had simple exact expressions. He used expansions in eigenfunctions of the Laplace operator (trigonometric polynomials). Platzman (1960) used the Galerkin method to study the planetary barotropic vorticity equation with as a basis the eigenfunctions on the sphere (spherical surface harmonics; Silberman (1954) was the first to do this) and showed the invariance of enstrophy at any truncation. This result depends on certain anti-symmetry properties of the interaction coefficients which follow directly from the vorticity equation and its projection (see also Thompson 1972). Below we closely follow Platzman's (1960) analysis which shows that enstrophy will be conserved at any truncation, even when not using eigenfunctions of the Laplace operator. Next we derive relation (A 7c); this is based on Kraichnan's (1958) approach where a triad interaction is considered. We introduce the following notation. The expansion of vorticity (9) is written as $\omega = \sum_\gamma b_\gamma \varphi_\gamma$, where $\gamma = r + im$. Thus, $b_r^m \equiv b_\gamma, \varphi_r^m \equiv \varphi_\gamma$. The complex index γ takes its values on the lattice of integer coordinates (r,m) on the right-hand side of the complex plane, including the points on the vertical axis $(r = 0)$. The φ are as in (12). For every γ used in the upper right quadrant, the complex conjugate $\gamma^\star$ in the lower half quadrant is also included (reality condition on ω). In vector notation equation (8) is

$$\frac{\partial \omega}{\partial t} = -\boldsymbol{u} \cdot \nabla \omega.$$

(B 1)

As is well-known, enstrophy is conserved:

$$\frac{\mathrm{d}}{\mathrm{d}t} \int\!\!\int_{\mathbf{R}^2} \omega^2 \mathrm{d}x\mathrm{d}y = \frac{\mathrm{d}}{\mathrm{d}t} \sum_\gamma |b_\gamma|^2 = 0. \tag{B 2}$$

This is at infinite resolution, i.e. γ takes all values on the lattice on the right-hand side of the complex plane. Projecting (B 1) according to (10), and substituting the ω-expansion we find

$$\frac{\mathrm{d}b_\gamma}{\mathrm{d}t} = \sum_\beta b_\beta \mathrm{M}_{\gamma,\beta}, \quad \mathrm{M}_{\gamma,\beta} = -\int\!\!\int_{\mathbf{R}^2} \varphi_\gamma^\star (\boldsymbol{u}\cdot\nabla\varphi_\beta)\mathrm{d}x\mathrm{d}y, \tag{B 3}$$

where β is a complex index like γ, which takes the same values as γ does. A single term in (B 2) is

$$\frac{\mathrm{d}}{\mathrm{d}t}|b_\gamma|^2 = b_\gamma \frac{\mathrm{d}b_\gamma^\star}{\mathrm{d}t} + b_\gamma^\star \frac{\mathrm{d}b_\gamma}{\mathrm{d}t} = b_\gamma \sum_\beta b_\beta^\star \mathrm{M}_{\gamma,\beta}^\star + b_\gamma^\star \sum_\beta b_\beta \mathrm{M}_{\gamma,\beta} \equiv \sum_\beta \mathrm{D}_{\gamma,\beta}.$$

By partial integration, using $\nabla\cdot\boldsymbol{u} = 0$ (incompressibility or $\boldsymbol{u} = \nabla\wedge\boldsymbol{k}\psi$, with ψ a streamfunction and $\boldsymbol{k}$ a unit vector normal to the plane of flow), and the vanishing of the φ at infinity, it follows from (B 3) that $\mathrm{M}_{\gamma,\beta} = -\mathrm{M}_{\beta,\gamma}^\star$ and consequently $\mathrm{D}_{\beta,\gamma} = -\mathrm{D}_{\gamma,\beta}$. Due to this anti-symmetry

$$\frac{\mathrm{d}}{\mathrm{d}t} \sum_\gamma |b_\gamma|^2 = \sum_\gamma \sum_\beta \mathrm{D}_{\gamma,\beta} = 0. \tag{B 4}$$

But, this is also true when $\{\gamma, \beta\}$ take values only in a finite set of lattice points. Therefore the truncated dynamics will conserve enstrophy. The non-trivial property (A 7c) of the interaction coefficients is found as follows. For convenience we rewrite the dynamics (11) as

$$\frac{\mathrm{d}b_\gamma}{\mathrm{d}t} = \sum_\alpha \sum_\beta I_{\gamma,\alpha,\beta} b_\alpha b_\beta, \quad I_{\gamma,\alpha,\beta} \equiv -\mathrm{i}I\begin{pmatrix} m & k & l \\ r & p & q \end{pmatrix}, \tag{B 5}$$

with the same notation as above, i.e. $\alpha = p + \mathrm{i}k, \beta = q + \mathrm{i}l, \gamma = r + \mathrm{i}m$. For a given γ at infinite resolution the double sum is over all lattice points α, β with the constraint $k + l = m$. Kraichnan (1958) argued as follows. We know that enstrophy is conserved at infinite resolution. But, an arbitrary initial condition can be assigned to the vorticity field. Consider a field represented by a triplet of expansion coefficients $\{b_\gamma, b_\alpha, b_\beta\}$, subject to the constraint $m = k + l$. Then, at $t = 0$

$$\frac{\mathrm{d}}{\mathrm{d}t}\left(|b_\alpha|^2 + |b_\beta|^2 + |b_\gamma|^2\right) = 0. \tag{B 6}$$

The left-hand side of (B 6) is equal to the sum of the following terms

$$\left.\begin{aligned}
b_{\gamma^\star}\frac{\mathrm{d}b_\gamma}{\mathrm{d}t} + \text{c.c.} &= I_{\gamma,\alpha,\beta}b_\alpha b_\beta b_{\gamma^\star} + I_{\gamma^\star,\alpha^\star,\beta^\star}b_{\alpha^\star}b_{\beta^\star}b_\gamma, \\
b_{\alpha^\star}\frac{\mathrm{d}b_\alpha}{\mathrm{d}t} + \text{c.c.} &= I_{\alpha,\gamma,\beta^\star}b_\gamma b_{\beta^\star}b_{\alpha^\star} + I_{\alpha^\star,\gamma^\star,\beta}b_{\gamma^\star}b_\beta b_\alpha, \\
b_{\beta^\star}\frac{\mathrm{d}b_\beta}{\mathrm{d}t} + \text{c.c} &= I_{\beta,\gamma,\alpha^\star}b_\gamma b_{\alpha^\star}b_{\beta^\star} + I_{\beta^\star,\gamma^\star,\alpha}b_{\gamma^\star}b_\alpha b_\beta,
\end{aligned}\right\} \tag{B 7}$$

where we used $b_\gamma^\star = b_{\gamma^\star}$. Using (A 7b), we find that (B 6) implies

$$\left[I_{\gamma,\alpha,\beta} - I_{\alpha,\gamma,\beta^\star} - I_{\beta,\gamma,\alpha^\star}\right]\left(b_\alpha b_\beta b_{\gamma^\star} - b_{\alpha^\star}b_{\beta^\star}b_\gamma\right) = 0. \tag{B 8}$$

In general the term in the square brackets must therefore vanish, or

$$I_{\gamma,\alpha,\beta} = I_{\alpha,\gamma,\beta^\star} + I_{\beta,\gamma,\alpha^\star}, \tag{B 9}$$

which is relation (A 7c). In some special cases the term $(\cdots)$ in (B 8) vanishes identically. It vanishes when (i) b_γ is real (zero azimuthal wavenumber) and the other two are each others complex conjugate, or (ii) b_α (b_β) is real and b_β (b_α) is equal to b_γ. Case (i) is when $\alpha = p + \mathrm{i}m, \beta = p - \mathrm{i}m, \gamma = r + \mathrm{i}0$, with arbitrary $p, r \geqslant 0$ and arbitrary m. Case (ii) is when $\alpha = p + \mathrm{i}0, \beta = r + \mathrm{i}m, \gamma = r + \mathrm{i}m$. In both cases it follows with (A 7a) and (A 7b) that (A 7c) still holds.

Note Added in Proof

It has come to our attention that G. J. F. van Heijst and M. Beckers (personal communication) have recently been able to create a square vortex in the laboratory.

REFERENCES

BATCHELOR, G. K. 1967 *An Introduction to Fluid Dynamics.* Cambridge University Press.

BECKERS, M. & HEIJST, G. J. F. VAN 1998 The observation of a triangular vortex in a rotating fluid. *Fluid Dyn. Res.* **22**, 265–279.

BENZI, R., PATARNELLO, S. & SANTANGELO, P. 1988 Self–similar coherent structures in two-dimensional decaying turbulence. *J. Phys.* A: *Math. Gen.* **21**, 1221–1237.

CARNEVALE, G. F. & KLOOSTERZIEL, R. C. 1994 Emergence and evolution of triangular vortices. *J. Fluid Mech.* **259**, 305–331.

CARNEVALE, G. F. & SHEPHERD, T. G. 1990 On the interpretation of Andrew's theorem. *Geophys. Astrophys. Fluid Dyn.* **51**, 1–17.

CARTON, X., FLIERL, G. R. & POLVANI, L. 1989 The generation of tripoles from unstable axisymmetric isolated vortex structures. *Europhys. Lett.* **9**, 339–344.

CARTON, X. & LEGRAS, B. 1994 The life-cycle of tripoles in two-dimensional incompressible flows. *J. Fluid Mech.* **267**, 53–82.

CARTON, X. & MCWILLIAMS, J. C. 1989 Barotropic and baroclinic instabilities of axisymmetric vortices in a quasi-geostrophic model. In *Mesoscale/Synoptic Coherent Structures in Geophysical Turbulence* (ed. J. C. J. Nihoul & B. M. Jamart), pp. 225–244. Elsevier.

DAVIDSON, P. A. 1998 On the application of the Kelvin-Arnol'd energy principle to the stability of forced two-dimensional inviscid flows. *J. Fluid Mech.* **356**, 221–257.

DRAZIN, P. G. & REID, W. H. 1981 *Hydrodynamic Stability.* Cambridge University Press.

DRITSCHEL, D. G. 1988 Nonlinear stability bounds for inviscid, two-dimensional, parallel or circular flows with monotonic vorticity, and the analogous three-dimensional quasi-geostrophic flows. *J. Fluid Mech.* **191**, 575–581.

FLOR, J. B. & HEIJST, G. J. F. VAN 1996 Stable and unstable monopolar vortices in a stratified fluid. *J. Fluid Mech.* **311**, 257–287.

GENT, P. R. & MCWILLIAMS, J. C. 1986 The instability of circular vortices. *Geophys. Astrophys. Fluid Dyn.* **35**, 209–233.

HEIJST, G. J. F. VAN & KLOOSTERZIEL, R. C. 1989 Tripolar vortices in a rotating fluid. *Nature,* **338**, 569–571.

HEIJST, G. J. F. VAN, KLOOSTERZIEL, R. C. & WILLIAMS, C. W. M. 1991 Laboratory experiments on the tripolar vortex in a rotating fluid. *J. Fluid Mech.* **225**, 301–331.

HIGGINS, J. R. 1977 *Completeness and Basic Properties of Sets of Special Functions.* Cambridge University Press.

KLOOSTERZIEL, R. C. & CARNEVALE, G. F. 1992 Formal stability of circular vortices. *J. Fluid Mech.* **242**, 249–278.

KLOOSTERZIEL, R. C. & HEIJST, G. J. F. VAN 1991 An experimental study of unstable barotropic vortices in a rotating fluid. *J. Fluid Mech.* **223**, 1–24.

KRAICHNAN, R. H. 1958 Irreversible statistical mechanics of incompressible hydromagnetic turbulence. *Phys. Rev.* **109**, 1407–1422.

LEGRAS, B., SANTANGELO, P. & BENZI, R. 1988 High–resolution numerical experiments for forced two-dimensional turbulence. *Europhys. Lett.* **5**, 37–42.

LORENZ, E. N. 1960 Maximum simplification of the dynamic equations. *Tellus* **12**, 243–254.

LORENZ, E. N. 1963 Deterministic non-periodic flow. *J. Atmos. Sci.* **20**, 130–141.

McCALPIN, J. D. 1987 On the adjustment of azimuthally perturbed vortices. *J. Geophys. Res.* **92**, 8213–8255.

McWILLIAMS, J. C. 1984 The emergence of isolated coherent vortices in turbulent flow. *J. Fluid Mech.* **146**, 21–43.

MOREL, Y. & CARTON, X. 1994 Multipolar vortices in two-dimensional incompressible flow. *J. Fluid Mech.* **267**, 23–51.

ORLANDI, P. & HEIJST, G. J. F. VAN 1992 Numerical simulations of tripolar vortices in 2D flow. *Fluid Dyn. Res.* **9**, 170–206.

PATTERSON, G. S. & ORSZAG, S. A. 1971 Spectral calculations of isotropic turbulence: Efficient removal of aliasing errors. *Phys. Fluids* **14**, 2438–2541.

PINGREE, R. D. & LE CANN, B. 1992 Anticyclonic eddy X91 in the Southern Bay of Biscay, May 1991 to February 1992. *J. Geophys. Res.* **97**, 14353–14367.

PLATZMAN, G. W. 1960 The spectral form of the vorticity equation. *J. Metl.* **17**, 635–644.

PRESS, W. H., FLANNERY, B. P., TEUKOLSKY, S. A. & VETTERLING, W. T. 1989 *Numerical Recipes: the Art of Scientific Computing.* Cambridge University Press.

SADOURNY, S. 1985 Quasi-geostrophic turbulence: an introduction. In *Turbulence and Predictability in Geophysical Fluid Dynamics and Climate Dynamics* (ed. M. Ghil), pp. 133–158.

SILBERMAN, I. S. 1954 Planetary waves in the atmosphere. *J. Metl.* **11**, 27–34.

THOMPSON, P. D. 1972 Some exact statistics of two-dimensional viscous flow with random forcing. *J. Fluid Mech.* **55**, 711–717.